Remote Sensing of Environment 252 (2021) 112126

Contents lists available at ScienceDirect

Remote Sensing of Environment

journal homepage: www.elsevier.com/locate/rse

Identifying relative strengths of SMAP, SMOS-IC, and ASCAT to capture temporal variability

Runze Zhang[a], Seokhyeon Kim[b,*], Ashish Sharma[b], Venkat Lakshmi[a]

[a] School of Engineering Systems and Environment, University of Virginia, Charlottesville, VA 22904, USA
[b] School of Civil and Environmental Engineering, University of New South Wales, Sydney, NSW 2052, Australia

ARTICLE INFO

Keywords:
Soil moisture
SMAP
SMOS-IC
ASCAT
Correlation coefficients
Optimal weights

ABSTRACT

This study evaluates the relative strengths of three remotely sensed soil moisture (SM) products to capture temporal variability at a global scale, the products being the Soil Moisture Active Passive (SMAP), Soil Moisture Ocean Salinity INRA-CESBIO (SMOS-IC) and Advanced Scatterometer (ASCAT). For this, the conventional reference-based Pearson correlation (R) and a statistical technique called Triple Collocation (TC)-based R are calculated. In addition, two alternatives for linear combination of the three data sources for maximizing R against the truth are evaluated, the first using a reference product (i.e. assumed truth) and the second based on TC where three data sources are combined without the need for an underlying reference or assumed truth. The estimated optimal combination weights represent quantitative contributions of the three products in forming the new combined product having the maximized R. Two reanalysis products: the European Centre for Medium-Range Forecast (ECMWF) Interim product (ERA-Interim) and the Modern-Era Retrospective Analysis for Research and Application Land version 2 reanalysis product (MERRA2), are used as the references as well as data alternatives to calculate the conventional reference-based R and the TC-based R combinations. Both types of R, and their derived optimal weights are then compared globally and analyzed under various climate, land cover, and vegetation conditions. Despite the differences between the conventional R and the TC-based R, both metrics displayed consistent spatial distributions and can reflect the temporal variations of each studied dataset without considerable impact from adopted references. All products had difficulty in retrieving SM over arid and polar regions while exhibiting good performance in areas such as South America and Australia. While ASCAT presented higher R values over tropical, savannas, and the vegetation water content interval of 2–5 kg/m^2, SMAP and SMOS-IC displayed overall comparable and continually high temporal performances across almost all conditions. In the case of the derived optimal weights, a global complementarity of the areas was observed where each satellite-based observation product showed its respective advantage in capturing SM variations in different geographic areas.

1. Introduction

Soil moisture (SM) is an important factor modulating both terrestrial-atmosphere interactions and hydrological circulation (Kerr et al., 2016; Srivastava et al., 2013; Van den Hurk et al., 2002). Given that SM provides useful information for many real-world applications, including flood and weather forecasting, there is an added significance of accurately estimating SM in both space and time (Entekhabi et al., 1999; Entekhabi et al., 1996).

Remote sensing has been considered as a promising technique for providing regional SM information at a global scale (De Jeu and EOwe, 2003; Kim et al., 2019; Petropoulos et al., 2015). Microwave remote sensors can measure the soil dielectric constant which is strongly correlated to the water content within the topsoil layer (Kerr et al., 2016; Pellarin et al., 2003). In comparison to optical/infrared radiation and analogous remote sensing alternatives (Kerr, 2007; Petropoulos et al., 2015), microwave remote sensing can operate under all-weather conditions and during night time (Srivastava et al., 2015). Additionally, microwave systems are less sensitive to surface roughness and can penetrate vegetation canopy (Ulaby et al., 1986; Wigneron et al., 1998). Due to their greater temporal resolution and lower influence by roughness disturbances than active sensors, passive microwave radiometers have been widely used to estimate SM since late the 1970's and form the focus of our investigation (Al-Yaari et al., 2014; Bertoldi et al., 2014; Kim et al., 2019).

Understanding error characteristics and limitations of SM retrievals

* Corresponding author.
E-mail address: seokhyeon.kim@unsw.edu.au (S. Kim).

https://doi.org/10.1016/j.rse.2020.112126
Received 9 April 2020; Received in revised form 27 August 2020; Accepted 3 October 2020

is an important step to improve retrieval algorithms. Given that, validation studies that evaluate the accuracy of the remotely-sensed SM products have been widespread and useful (Al-Yaari et al., 2019; Ma et al., 2019; Zhang et al., 2019). Errors in satellite SM data can be presented by statistical metrics (e.g. bias and root mean squared error). These errors generally result from uncertainties in the retrieval process and/or limitations of the satellite instruments, with uncertainties inevitably inducing biases and/or unreasonable dynamic ranges of the retrievals. Moreover, it is often hard to exactly evaluate satellite products due to the absence of references at spatial scale corresponding to those of the satellite data (Clewley et al., 2017; Crow et al., 2012). Consequently, the temporal Pearson correlation coefficient (R) has been considered as a comparatively reliable metric in the performance comparisons of spatially mismatched SM products (e.g. in-situ and remotely sensed SM retrievals). This is because it is less sensitive to the bias or amplitude of variations (Entekhabi et al., 2010b), and the temporal dynamics of SM is relatively stable over a large area compared to absolute values that are affected by the high variability of local SM (Brocca et al., 2009a). In addition, in many applications, the temporal variability in geophysical variables has been considered as an important statistic (Guillod et al., 2015; Gupta et al., 2006; Koster and Suarez, 2001) and scaling has been subsequently applied to adjust the range of variables before use in applications (Brocca et al., 2009b; Reichle et al., 2004; Yilmaz and Crow, 2013).

In view of this, this study uses Pearson correlation (R) to assess the temporal performances of SM retrievals derived from various satellite instruments. Two types of R including the conventional R calculated based on the arbitrary references and the R values derived using the triple collocation (TC) approach Stoffelen, (1998) were used and compared. For the conventional R, three different reference products have been selected, which are the in-situ measurements, and two reanalysis products: European Centre for Medium-Range Weather Forecast (ECMWF) ERA-Interim SM product and Modern-Era Retrospective Analysis for Research and Application Land version 2 reanalysis product (MERRA2).

Together with estimating R, we also evaluate the relevance of one data source compared to another using an optimal weight (w), to identify relative contributions of individual SM products to capture the temporal variability. Here, the optimal weight is defined as the weight (within its constrained range) of the parent product being linearly merged to maximize R between the combined product and an objective reference dataset (Hagan et al., 2020; Kim et al., 2018; Kim et al., 2015). In the linear combination scheme, the optimal weight can be interpreted as the quantitative contribution of each parent product.

Different from the R that indicates the absolute performance of the product with regard to the reference datasets, the optimal weight can reflect the dependent performances among the parent products relative to each other. Additionally, the optimal weight is expected to contain the unique strength of each parent product. This has been demonstrated by the improved performances of the combined product compared to individual parent product (Kim et al., 2015). In other words, when two parent products contain much overlapped information, the contribution from one product tends to largely reduce. In light of this, it is critical to investigate the relationship between the R and the optimal weights for further enhancing the quality of the combined products.

Using the two metrics, R and optimal weight, this study compared three high-quality SM products at a global scale: Soil Moisture Active Passive Level 3 (SMAP); Soil Moisture Ocean Salinity INRA-CESBIO (SMOS-IC); Advanced Scatterometer (ASCAT). Here, the study period is from April 2015 to March 2018, nearly double of recent related studies, providing more confidence in the conclusions made (Al-Yaari et al., 2019; Ma et al., 2019).

The paper is structured as follows. In Section 2, we describe the process to calculate the optimal weights and evaluation strategy, and Section 3 introduces the datasets used. Then we present and discuss the results in Section 4, based on the diverse static conditions. Finally, conclusions are presented followed by a summary in Section 5.

2. Methodology

2.1. Triple collocation-based data-truth correlation

Together with using the conventional R calculated based on the specified reference products, this study applied Triple Collocation (TC) to estimate the data-truth R. TC is an inter-comparison between three independent products which allows approximate estimation of the error variance of each product along with the correlation between each product and the unknown truth. The approximation in TC becomes possible with four assumptions: 1) linearity between the truth and the errors; 2) stationarity for both the truth and the error; 3) zero error cross-correlation; 4) error-truth orthogonality. Detailed equations and their derivations are available in Stoffelen (1998); McColl et al. (2014); Gruber et al. (2016). In this study, the data-truth correlations are estimated using Eq. (1).

$$R_{X,T} = \sqrt{\frac{Cov(XY)Cov(XZ)}{Cov(XX)Cov(YZ)}} \tag{1}$$

where $R_{X,T}$ represents the correlation between the product X and the TC-derived data truth (T). X, Y, and Z represent the different datasets within the triplet, and Cov means the covariance of any two studied products.

Following a typical combination of datasets used in TC approach (i.e. active, passive and modeling products) (Chen et al., 2018; Kim et al., 2018), we adopted two data triplets to estimate the TC-derived data-truth R of the satellite-based products, which are 1) SMAP, ASCAT and a reference product (i.e. in-situ observation, ERA-Interim and MERRA2 in this study), and 2) SMOS-IC, ASCAT and a reference product. For consistency in estimating the TC-based R, those for SMAP and ASCAT were extracted from the first triplet and that for SMOS-IC was estimated from the second triplet.

2.2. Estimating optimal weights for maximizing R

In this study, the relative contribution in capturing temporal SM variations was represented and compared using optimal weights in a linear combination scheme. The linear combination can effectively incorporate the advantages of each parent product and potentially generate a new product with better performance than any individual dataset being merged (Kim et al., 2015, 2016).

The SM dataset (n data length × p datasets) are linearly combined by assigning a weight vector $\boldsymbol{w}$ (p × 1) to the dataset to generate a combined product $\mathbf{SM}_c$ (n × 1) using Eq. (2).

$$\mathbf{SM}_c = \mathbf{SM} \times \boldsymbol{w} \tag{2}$$

The optimal weight ($\boldsymbol{w}^*$) can be obtained by solving a constrained optimization problem of maximizing the correlation between $\mathbf{SM}_c$ and the reference, i.e. R_{cr}, as

$$\boldsymbol{w} = \underset{\boldsymbol{w}}{\operatorname{argmax}} R_{cr}(\boldsymbol{w})$$

$$\text{subject to } 0 \le w_i \le 1, \sum_{i=1}^{p} w_i = 1 \tag{3}$$

The weight is able to effectively reflect the sensitivity of the combined product to the corresponding parent product, or the contribution an individual dataset makes in forming the combination.

In case of merging two products ($\mathbf{SM}_1$ and $\mathbf{SM}_2$) for which standard deviations are the same (i.e. scaled to each other or a reference), the optimal weights (w_1 and w_2) are affected by R between the two products (R_{12}) and the data-reference R (R_{1R} and R_{2R}) (Kim et al., 2015).

$$w_1 = \frac{R_{1R} - R_{12}R_{2R}}{(R_{2R} - R_{12}R_{1R}) + (R_{1R} - R_{12}R_{2R})}$$

$$w_2 = 1 - w_1 \tag{4}$$

In this study, when considering three products being merged for maximizing R, Eq. (5) was extended as per Kim et al. (2015).

$$w_1 = \frac{AS_2S_3}{CS_1S_2 + BS_1S_3 + AS_2S_3}$$

$$w_2 = \frac{BS_1S_3}{CS_1S_2 + BS_1S_3 + AS_2S_3}$$

$$w_3 = \frac{CS_1S_2}{CS_1S_2 + BS_1S_3 + AS_2S_3}$$

where,

$$A = R_{12}R_{2R} - R_{1R} + R_{13}R_{3R} + R_{23}^2R_{1R} - R_{12}R_{23}R_{3R} - R_{13}R_{23}R_{2R}$$

$$B = R_{12}R_{1R} - R_{2R} + R_{23}R_{3R} + R_{13}^2R_{2R} - R_{12}R_{13}R_{3R} - R_{13}R_{23}R_{1R}$$

$$C = R_{13}R_{1R} - R_{3R} + R_{23}R_{2R} + R_{12}^2R_{3R} - R_{12}R_{13}R_{2R} - R_{12}R_{23}R_{1R} \tag{5}$$

where the subscripts, 1, 2, 3 and R, represent the parent products being merged and the reference, and S_i represents the standard deviation of a given candidate.

In order to directly evaluate the product's contribution to capture temporal variability by removing effects from differences in standard deviations, all parent products were rescaled against a reference using Eq. (6) before calculating the optimal weights. Note that the R values among the newly yielded datasets and references would not be affected by the rescaling process.

$$\mathbf{SM}_{\text{rescaled}} = (\mathbf{SM}_{\text{raw}} - \overline{\mathbf{SM}_{\text{raw}}}) \times \frac{\text{std}(\mathbf{SM}_{\text{ref}})}{\text{std}(\mathbf{SM}_{\text{raw}})} + \overline{\mathbf{SM}_{\text{ref}}} \tag{6}$$

where $\mathbf{SM}_{\text{rescaled}}$, $\mathbf{SM}_{\text{raw}}$ and $\mathbf{SM}_{\text{ref}}$ represent the SM values of rescaled product, raw product, and reference, respectively. $\overline{\mathbf{SM}}$ and std(**SM**) are the average and standard deviation values of SM data.

As mentioned, the TC-based data-truth R has the ability to represent the correlation between the product and the SM truth. When the SM truth is identified as the objective dataset for the linear combination, the relative contribution of each parent product can be reflected by the optimal weights derived from the TC-based data-truth R. To distinguish the optimal weights obtained by adopting the arbitrary reference products and the SM truth as the targets of the combination products, the optimal weights computed from the conventional R and the TC-based R are referred to be as w_{con} and w_{TC}, respectively. While the TC assumptions are satisfied and the parent products have been processed by the rescaling process, Eq. (5) can be further simplified as:

$$w_{TC1} = \frac{R_{TC1}(1 - R_{TC2}^2)(1 - R_{TC3}^2)}{S}$$

$$w_{TC2} = \frac{R_{TC2}(1 - R_{TC1}^2)(1 - R_{TC3}^2)}{S} \tag{7}$$

$$w_{TC3} = \frac{R_{TC3}(1 - R_{TC1}^2)(1 - R_{TC2}^2)}{S}$$

$$S = R_{TC1}(1 - R_{TC2}^2)(1 - R_{TC3}^2) + R_{TC2}(1 - R_{1TC}^2)(1 - R_{TC3}^2) + R_{TC3}(1 - R_{TC1}^2)(1 - R_{TC2}^2)$$

R_{TCi} denotes Pearson correlation coefficients between product i and the SM truth using the TC approach.

According to Eq. (7), w_{TC} represents the contribution each product makes to the combination, expressed as a function of the various correlations needed in its specification. When considering Eq. (5) and Eq. (7) together, however, this compatibility between the TC-based data-truth R and w_{TC} can be distorted for the following two reasons: 1) R's occurring with opposite signs; and, 2) violations of the independence between the selected datasets (e.g. non-zero error cross-correlations). It should be noted that Eq. (7) cannot directly be used to derive w_{TC} when any of the underlying TC assumptions is not satisfied. In practice, these factors can also affect the consistency between the conventional R and w_{con}. As such, the consistency between the optimal weights and the R values and the impacts of the error cross-correlations on their consistency were further explored by a set of synthetic experiments described in Appendix.

2.3. Evaluation strategy

To identify the areas of relative performance for each parent product, evaluations and comparisons were performed at two levels: overall and conditioned by surface conditions. In addition, the consistency between the TC-derived data-truth R and the conventional R, and between the R values and the corresponding optimal weights in performance sequence has been separately assessed to increase the reliability of obtained results.

Specifically, we first compared the distributions of the conventional R and the TC-based R for all the parent products at a global scale. The characteristics of the temporal performance for each satellite-based SM dataset were further investigated across various static conditions including climate and land cover classes, and mean vegetation water contents. The reasons behind the similarity and difference of temporal performances described by the above two R types were studied and discussed. It should be stressed that the comparisons about the conventional R and the TC-based R are performed and summarized by applying three different reference products (in-situ measurements, ERA-Interim, and MERRA2 in supplementary material).

Given the SM retrievals derived from the discrete satellite observations over the studying period, the evaluation results for the remotely-sensed products are prone to certain uncertainties resulting from sampling errors. Due to the strong autocorrelation in the SM data, the optimum block lengths commonly used in the moving block bootstrapping are almost identical to the study period while that of SM anomalies becomes to several days (Chen et al., 2018). Therefore, we calculated the confidence intervals (CI) by simply using randomly selected 100 of 1-year blocks over the study period by which the seasonality effects on the uncertainty can be ignored. For this we assumed that the interannual variability over the 3-year period is ignorable. Here, the CIs were still estimated using the differences between the 97.5th and 2.5th percentiles of the R values obtained in the repeated simulations to demonstrate the reliability of results.

In terms of the relative performance, the consistency between the R and its derived optimal weight was analyzed via a set of synthetic experiments and the results are available in Appendix. Additionally, the impacts of the error cross-correlations on the numerical values of the optimal weights were also investigated to improve the interpretation of the relationship between the optimal weight and the R. Using the reference products and the SM truth as the combination objectives, the global distributions of the optimal weights calculated using the conventional R and the TC-based R were demonstrated and compared.

3. Data

As summarized in Table 1, various datasets covering the 3-year study period (April 1, 2015- March 31, 2018) have been used in this study. These include 1) three satellite-derived SM products as parent products: SMAP, SMOS-IC, and ASCAT; 2) two reanalysis products as references: ERA-Interim and MERRA2; 3) three static conditions: climate zone (CZ), land cover (LC) and mean vegetation water content (VWC). Additionally, in-situ SM measurements from 131 stations of the International Soil Moisture Network (ISMN) (Dorigo et al., 2011) were also selected as the reference dataset. (See Fig. 1 and Table 3.)

Note that a common spatial resolution of 36 km × 36 km was adopted for all datasets used in this study based on the global cylindrical 36 km Equal-Area Scalable Earth, version 2 (EASEv2) (Brodzik

Table 1
Summary of datasets used in this study.

Data	Data source and/or product name	Reference	Resolution (temporal/spatial)	Unit
Satellite SM	SMAP L3 soil moisture product (Version 5)	O'Neill et al. (2018)	Daily, overpass (asc/des) at 6 PM/AM LST /36-km EASE-Grid	m^3/m^3
	SMOS-IC soil moisture product (Version 105)	Fernandez-Moran et al. (2017a); Fernandez-Moran et al. (2017b)	Daily, overpass (asc/des) at 6 AM/PM LST /25-km EASE-Grid	m^3/m^3
	ASCAT L2 soil moisture index product (Version 5)	Wagner et al. (2013); Naeimi et al. (2009)	Daily, overpass (asc/des) at 9:30 PM/AM LST /25 km	degree of saturation (0–100%)
Reference SM	MERRA2 topsoil layer soil moisture consent SFMC (M2T1NXLND) * in supplementary materials	Reichle et al. (2017)	Hourly(time-averaged)/0.5° × 0.625°	m^3/m^3
	ERA-Interim volumetric soil water layer 1	Dee et al. (2011)	6-hourly/25 km	m^3/m^3
	131 stations from the ISMN	Dorigo et al. (2011)	Hourly/point	m^3/m^3
CZ	Updated world map of the Köppen-Geiger climate classification	Peel et al. (2007)	−/0.25°	–
LC	MODIS(MCD12Q1)	NASA-LP-DAAC (2012)	Yearly/0.05°	–
VWC	SMAP VWC (SPL3SMP_E)	Chan et al. (2013)	Daily/9 km	kg/m^2

where asc/des: ascending/descending; LST: local solar time; EASE: Equal-Area Scalable Earth. SMAP, MERRA2 and MODIS products are available from the NASA Earthdata website (https://earthdata.nasa.gov/); SMOS-IC:https://www.catds.fr/Products/Available-products-from-CEC-SM/SMOS-IC; ASCAT: https://www.eumetsat.int/website/home/Data/index.html;

et al., 2012). To this end, all data from the products where spatial resolutions do not conform with the common resolution, were resampled using the bilinear interpolation unless otherwise stated. Additionally, a minimum number of corresponding observations over the studying period has been set as 50. For the SM data from the hourly updated reference datasets (i.e. ERA-Interim, MERRA2, and the in-situ observations), only the data that are closest to 6 a.m. local solar time (LST) were retained. Given that the ASCAT SM retrievals are based on the observations collected at 9:30 a.m. LST, the assessment of the performance of the ASCAT product are likely to be partially underestimated.

3.1. Satellite soil moisture products

3.1.1. SMAP

With the aim of mapping the global SM and monitoring the landscape freeze/thaw conditions, the SMAP satellite was launched in January 2015 by National Aeronautics Space Administration (NASA) (Entekhabi et al., 2010a). To incorporate advantages of both active and passive microwave sensors, SMAP satellite carries a radar (1.26 GHz) and a radiometer (1.41 GHz) operated at the L-band frequency but its radar stopped working in July 2015 due to a hardware malfunction. The nominal spatial resolution of the SMAP radiometer that observes the brightness temperature at the constant 40° incidence angle. Orbiting in a near-polar sun-synchronous track at the altitude of 685 km, the scanning time of the SMAP radiometer is around 6 a.m. LST (descending) and 6 p.m. LST (ascending). In addition to surface SM products, the SMAP mission can also provide root-zone SM, freeze/thaw conditions, and the net exchange of carbon.

In this study, a descending SMAP L3 Radiometer Global Daily 36 km Equal-Area Scalable Earth (EASE) Grid Soil Moisture (SPL3SMP, hereafter simply referred to as SMAP) has been used. Using the similar criteria applied in previous studies (Zhang et al., 2019), the SMAP SM data retrieved under the following conditions were consistently filtered out: 1) the SM retrievals within the grids where the percentages of the open water area are larger than 10%; 2) SM data obtained from the areas where VWC higher than 5 kg/m^2; 3) the SM retrievals in the pixels where the fraction of the frozen condition (LST < 273.15 K) is larger than 10%; 4) not recommended by the retrieval quality flag.

3.1.2. SMOS-IC

The SMOS satellite launched by European Space Agency carries the first L-band (1.4 GHz) interferometric radiometer to provide multi-angular and dual-polarization measurements of brightness temperature for global SM and vegetation optical depth mapping (Kerr et al., 2001). The spatial resolution of the SMOS sensor is around 43 km (Kerr et al., 2012). Operating in a sun-synchronous orbit, the crossing times at the equator of the satellite are 6 a.m. LST for ascending pass and 6 p.m. LST for descending pass (Fernandez-Moran et al., 2017a). Based on the L-band Microwave Emission of the Biosphere model (Wigneron et al., 2007), the gridded SM retrievals and vegetation optical depths can be estimated by a cost function to minimize the difference between the modeled and observed brightness temperatures (Wigneron et al., 2000).

The SMOS-IC product developed by INRA (Institute National de la

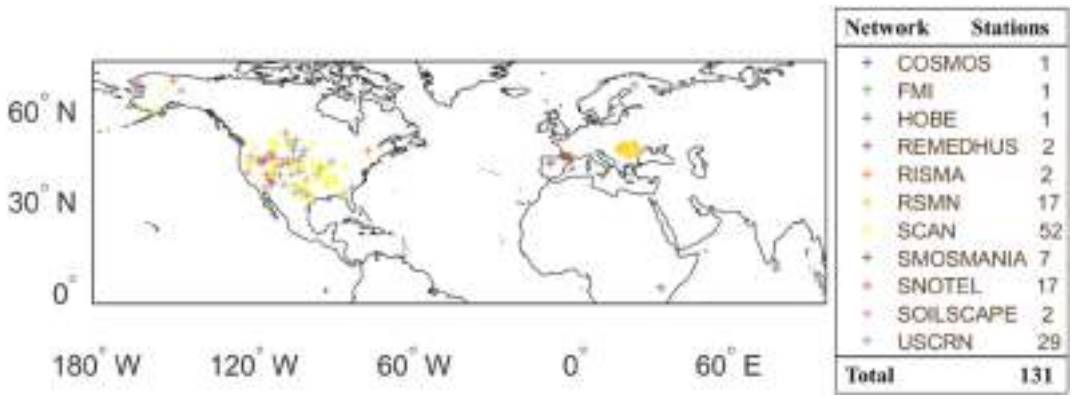

Fig. 1. The distribution of the 131 ISMN stations used for this study.

Recherche Agronomique) and CESBIO (Centre d'Etudes Spatiales de la BIOsphere) provides surface SM retrievals posted into the 25 km EASE grids at a global scale (Fernandez-Moran et al., 2017b; Li et al., 2020). There are four main differences in the processes of retrieving SM and vegetation optical depth data for the previous SMOS products (i.e. SMOS L2 and L3 datasets) and the SMOS-IC (Fernandez-Moran et al., 2017b). Firstly, the SMOS-IC algorithm assumes that each pixel is homogeneous instead of considering the LC details (4 km × 4 km) within the grid as the SMOS-L2 and L3 algorithms did. By retrieving the SM and vegetation optical depth over a homogeneous grid rather than deriving the representative pixel SM from the dominant fraction part, SMOS-IC retrievals become independent from the auxiliary datasets including European Centre for Medium-Range-Weather Forecast (ECMWF) SM and Moderate Resolution Imaging Spectroradiometer (MODIS) Leaf Area Index (LAI) to reduce the excess error propagations. Thirdly, new values of effective vegetation scattering albedo and soil roughness parameters (Parrens et al., 2016) based on the International Geosphere-Biosphere Programme (IGBP) classification have been used in the SMOS-IC algorithm after deliberated calibrations and validations (Fernandez-Moran et al., 2017a). Furthermore, the SMOS-IC algorithm selects the SMOS L3 brightness temperature product as the main input for SM and vegetation optical depth retrievals. The adoption of this optimized brightness temperature dataset does not account for the corrections of antenna patterns associated with the viewing angles and azimuth thus improving the computing efficiency (Fernandez-Moran et al., 2017a). To guarantee the quality of SMOS-IC SM retrievals, only the data with 'recommended quality' were retained and adopted here. In addition, the scene flags no more than 1 (SF ≤ 1) and the TB-RMSE ≤ 8 K have also been applied to further remove uncertain SMOS-IC data possibly interfered by the local conditions and strong RFI (radio frequency interference) impacts.

3.1.3. ASCAT

ASCAT is a real aperture radar currently flown onboard the Meteorological Operational A and B satellites (MetOp-A and MetOp-B) which fly in a near-polar sun-synchronous orbit at the altitude of 817 km (Wagner et al., 2013). With a spatial footprint varying from 25 km to 34 km, ASCAT sensors are operated at the C-band (5.255 GHz) in a VV polarization. Three antennas (on each side of the satellite) illuminate a wide swath of 550 km and receive quasi instantaneous backscatter power measurements at 3 different azimuth angles and two different incidence angles (Wagner et al., 2013). The equatorial overpass time of the ASCAT is 9:30 a.m. and 9:30 p.m. for the descending and ascending orbits, respectively. The retrieval of the relative SM (i.e. degree of saturation) from ASCAT measured backscatter coefficients is based on a semi-empirical change detection method (Hahn, 2016; Naeimi et al., 2009). Here, the descending MetOp-B ASCAT soil moisture 25 km sampling Near Real-Time (Version 5) within the grids where the probability of snow and frozen ground below 10%, and the SM estimated retrieval errors below 50%, were selected (Chen et al., 2018).

3.1.4. Key differences in soil moisture retrieval algorithms

Regarding the three candidates being compared, SMAP and SMOS-IC use brightness temperatures observed from the L-band passive microwave sensors and retrieve SM values using the zero-order radiative transfer model (Mo et al., 1982; Wigneron et al., 2017). ASCAT with active C-band radar can measure the backscatter coefficient and derive the relative SM content using a semi-empirical changing detection method (Wagner et al., 1999). As summarized in Table 2, in this study, the key differences in the retrieval algorithms of the SMAP, SMOS-IC and ASCAT are categorized into parameterizations of physical temperature, surface roughness, vegetation, and dielectric mixing models used convert obtained dielectric constants to SM values.

3.2. ISMN soil moisture data

The in-situ SM data of 131 stations from 11 networks were used in this study as a reference to calculate the conventional R and as a critical component of the triplets to estimate the TC-derived data-truth R. These stations mostly distributed over North America, Alaska, Europe, and Asia. Following the same filtering procedures used in Zhang et al. (2019), the stations where in-situ SM measured at a shallowest depth smaller than 10 cm and symbolized as 'good' in the quality flag were retained. Additionally, the pixels in which the proportions of the topographic complexity and wetland fraction are less than 10% were considered. To avoid an uneven high weight for the pixels, only in-situ SM data from one station was selected to represent SM variations in one grid. In light of this, the stations with the highest average conventional R with the satellite-based SM products considered here were used when multiple stations locate in the same grid (Dorigo et al., 2015). Given that Colliander et al. (2018) has shown that SM observations over 9 km and 33 km are approximated in depicting the SM temporal variations, the SM averages of in-situ measurements are assumed to be able to represent the areal SM variations at 36 km and have marginal effects on the estimated correlations with the satellite-based products.

4. Results and discussion

4.1. Comparisons of conventional and TC-based R over in-situ stations

The in-situ SM data were used as the reference to calculate the conventional R for each parent product. In addition, two triplets containing the in-situ SM data (i.e. SMAP, ASCAT, in-situ SM; SMOS-IC, ASCAT, in-situ SM) were also adopted to derive the TC-based data-truth R of the satellite-based products. The above two types of R values were referred to as 'in-situ conR' and 'in-situ TCR' to distinguish from the conventional R (conR) and the TC-based data-truth R (TCR) calculated based on the reanalysis products (ERA-Interim, here). Using the in-situ conR as the benchmark, the absolute values of the differences (ΔR) between different types of R values and the in-situ conR were separately computed over the pixels with the in-situ stations.

As shown in Fig. 2, ΔR values are generally distributed around 0.2 for each parent product. Despite the inclusion of the in-situ SM data in the triplet, it is to be noted that ΔR values for the in-situ TCR (D1 in Fig. 2) tend to be similar or even higher than those for the TCR (D3 in Fig. 2) across all SM products. The analogous performances of the in-situ TCR and the TCR could be attributed to the similar SM variations captured by the ERA-Interim and the in-situ SM data, which is also demonstrated by the smaller differences (~ 0.1) between the conR and the in-situ conR (D2). As shown in Fig. 2, the conR is expected to be more reliable over the studying places due to the smaller bias with the in-situ conR while directly using the raw SM data.

The TCR is theoretically more reliable than the conR because the conR is highly dependent on the quality of the references (Gruber et al., 2016). However, the results in Fig. 2 indicate that the superiority of TCR is not always guaranteed in practice. The TCR based on a triplet can be also degraded because of several factors. In addition to violating some of the TC assumptions (e.g. zero error cross-correlation), different signs and considerably different qualities of the datasets collocated in the triplet could also degrade the quality of the TCR. Rather, if the quality of the references is good enough, the conR could be even better than the TCR as D2 < D1 and D3 in Fig. 2.

4.2. Global maps of correlation

Fig. 3 presents the global distribution of the conR and the TCR of the three SM products (SMAP, SMOS-IC, and ASCAT) and their differences.

The global distributions of conR (Fig. 3a–c) and TCR (Fig. 3d–f) are generally consistent in their respective spatial patterns. In view of the areas where both types of R are commonly noted, all three products

Table 2
Summary of key differences among the SMAP L3, SMOS-IC, and ASCAT retrieval algorithms.

Algorithm	SMAP L3 (SCA-V)	SMOS-IC (L-MEB)	ASCAT (TU Wien Change Detection)
Observation	T_B (V-polarization) at a fixed incidence angle of 40°	Multi-angular and dual polarization SMOS L3 T_B	Multi-angular and VV-pol backscatter coefficient σ^0
Physical Temperature	· $T_s = T_c$, derived from GEOS-5 model surface and depth products. · $C_T = 0.246$	· $T_s(T_c)$ derived from ECMWF skin temperature (soil temperature of 0–7 cm topsoil layer). · $C_T = \left(\frac{SM}{W_0}\right)^{b_0}$, $W_0 = 0.3\ m^3/m^3$; $b_0 = 0.3$	
Roughness Parameter	· H_R values from an IGBP class look-up table · $N_R = 2$ · $Q_R = 0$	· H_R values from Parrens et al. (2016) · $N_{RP} = -1$ (P = H, V) over low vegetation · $N_{RV} = -1$, $N_{RH} = 1$ over forests · $Q_R = 0$	· Roughness conditions are assumed to be stable over time · Slope σ′ and curvature σ″
Vegetation	· $\tau = b \cdot VWC$ · ω and b vary with land cover classes (IGBP) · VWC derived from MODIS NDVI values	· τ simultaneously computed with SM and its initial value is 0.5 · ω calibrated based on IGBP classifications	· Vegetation effects are considered on a seasonal scale-cross over angles θ_d and θ_w · Slope σ′ and curvature σ″ on a time-window basis · Land cover conditions are assumed to be stable over time
Dielectric mixing model	· Mironov et al. (2009)	· Mironov et al. (2009)	

T_B = brightness temperature; T_s = soil surface temperature; T_c = vegetation canopy temperature; GEOS-5: Goddard Earth Observing System Model, Version 5; C_T = parameters (Choudhury effective temperature scheme); W_0, b_0 = fitting parameters (Wigneron effective temperature scheme); τ = vegetation optical depth; b = vegetation parameter; Q_R = polarization mixing coefficient; H_R = roughness parameter; N_{RP} = roughness parameter accounting for polarization dependency; NDVI = normalized difference vegetation index; ω = effective scattering albedo; ECMWF: European Centre for Medium-Range-Weather Forecast; σ′ = slope parameter; σ″ = curvature parameter; θ_d = reference angle for dry condition; θ_w = reference angle for wet condition.

Table 3
Summary of in-situ SM used in this study.

Network	Country (Number of stations)	Reference
COSMOS	USA (1 station)	Zreda et al. (2008)
FMI	Finland (1 stations)	http://fmiarc.fmi.fi/
HOBE	Denmark (1 stations)	Bircher et al. (2012)
REMEDHUS	Spain (2 stations)	Sanchez et al. (2012)
RISMA	Canada (2 stations)	(Ojo et al., 2015)
RSMN	Romania (17 stations)	http://assimo.meteoromania.ro
SCAN	USA (52 stations)	http://www.wcc.nrcs.usda.gov/
SMOSMANIA	France (7 stations)	Albergel et al. (2008)
SNOTEL	USA (17 stations)	Leavesley et al. (2008)
SOILSCAPE	USA (2 stations)	Moghaddam et al. (2010)
USCRN	USA (29 stations)	Bell et al. (2013)
Total	131 stations	

* ISMN data are available from: https://ismn.geo.tuwien.ac.at. Where, Unit = m^3/m^3, Resolution (temporal/spatial) = Hourly/point.

exhibit good temporal performance over North America, South America, the middle and southern parts of Africa, and most parts in Australia. Compared to the passive remote sensing SM (SMAP and SMOS-IC), the ASCAT product has considerably low conR values (Fig. 3c) over part of the Middle East where the TCR values of ASCAT are almost at the same magnitudes as SMAP and SMOS-IC's. When using the MERRA2 as the reference (Fig. S2 in supplementary material), similar distribution patterns of its conR and TCR can be found for those satellite-based products.

However, regardless of the conR or the TCR, the temporal performance of SMAP, SMOS-IC, and ASCAT is relatively low in North Africa which is typically defined as arid and semi-arid environments. Over such regions, microwave sensors are likely to suffer challenges in observing relevant signals (Dorigo et al., 2010; Kim et al., 2018). One possible error is the inaccurate estimation of the radiating soil depth and the effective temperature since low-frequency microwave radiation could penetrate deeper soil layer (Holmes et al., 2006; Kim et al., 2018). Moreover, the SM variations within the extremely dry regions are too small to detect by the scanning instrument or even interfere with the instrument noises. Compared to the SM retrieved from the passive observations, the ability of ASCAT to capture the SM temporal variability over arid and semi-arid areas is relatively lower (more blue areas). The opposing correlations between the modeling products and the active SM retrievals can be attributed to the backscatter returns dominated by the local sub-surface structure and collection geometry in the arid environment (Morrison and Wagner, 2019).

In the high latitude areas (i.e. north part of North America, northern Europe, and northeastern Asia), the parent SM products do not have good agreements, especially for the conR values shown in Fig. 3a–c. Similarly, the TCR values of SMAP, SMOS-IC, and ASCAT also moderately reduced. The relatively higher density of soil organic matter over the high latitude areas may account for the low correlations (De Lannoy et al., 2014). The temperature might not be the primary factor to reduce the correlations between the SM retrievals derived from passive

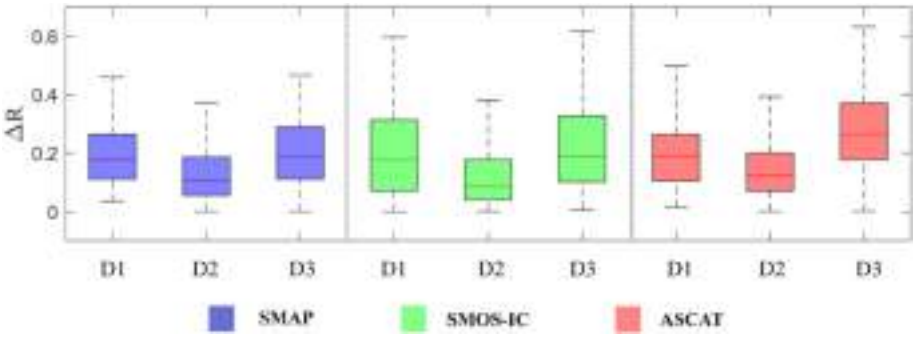

Fig. 2. Boxplot of Δ*R*, the absolute values of differences between in-situ conR and the three types of R: in-situ TCR (D1 = |in-situ TCR – in-situ conR|), conR (D2 = |conR- in-situ conR|)and TCR (D3 = |TCR-in-situ conR|).

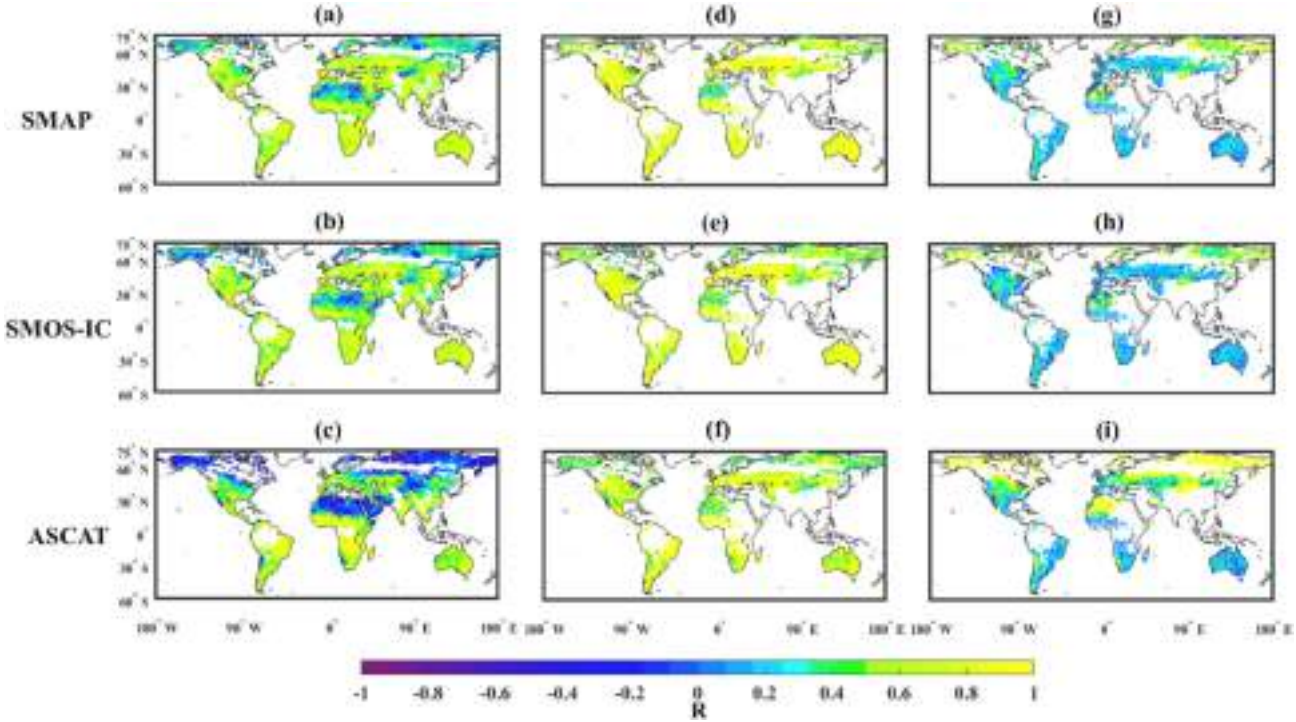

Fig. 3. Global distribution of conventional R for SMAP, SMOS-IC, and ASCAT using ERA-Interim as reference (a-c), and the TC-based R using ERA-Interim as the component of triplets (d-f). The second column "minus" the first column (g-i).

microwave observations and the reference products because ECMWF and Goddard Earth Observing System Model, Version 5 (GEOS-5) surface temperature products have been validated with high temporal correlations with the in-situ measurements over almost all climate conditions (Ma et al., 2019). Moreover, the retrieval of SM from active microwave observations is less sensitive to surface temperature variations.

However, differences between the conR and the TCR commonly exist and are around positive 0.2 over most regions (Fig. 3g–i). The larger deviations in the high-latitude areas and North Africa are possibly caused by the opposite signs of R values. In addition, the distributions of the products with the highest TCR and conR values are different over their overlapping pixels. For example, the proportion of grids in which the ASCAT product has a relatively superior temporal performance than SMAP and SMOS-IC are around 27% (for TCR) and 15% (for conR). Moreover, the number of grids with effective TCR is only around 40% of that of pixels with the valid conventional R, which can also be clearly observed in Fig. 3. Furthermore, the number of pixels with the highest TCR values of SMOS-IC is half of the number of grids with the highest conR values of the same product. Such discrepancies are partly caused by the reversed correlation signs of the TCR and the conR values, especially in the high-latitude regions for ASCAT. In light of this, for ASCAT, the spatial correlation between the TCR and conR is only 0.56 while those for SMAP and SMOS-IC are moderately higher (0.62 for SMAP; 0.71 for SMOS-IC).

The possible reasons that lead to the differences between the conR and TCR values can be summarized as the violation of TC assumptions, the sign effect, and sampling numbers. Theoretically, while the TC assumptions are fully satisfied, the TCR is expected to be more accurate because the use of conR involves added contribution from the reference product (Gruber et al., 2016). In practice, however, the TC related assumptions are more or less violated in particular when the data from satellite-observation datasets and the land surface modeling products are directly adopted. In terms of calculation equations related to TCR (Gruber et al., 2016; McColl et al., 2014), the non-zero error cross-correlations can straightforwardly affect the R values (Yilmaz and Crow, 2014).

The sign compatibility between the observation products and the truth needs to be carefully considered. Additionally, when the SM temporal variations described by one dataset are largely different from the other two products, the unreliable estimations of the TCR, such as the square TCR values larger than 1, would occur. Although the pixels with either negative or more than 1 square TCR values are commonly filtered out, the cases where two products are negatively correlated with the third one, likely exist and generate unsound TCR.

In addition, the reduction of the sample numbers due to the data collocation can also affect the TCR. The effective time-series data of the satellite-based SM product have to be curtailed to accommodate the TC requirements. Nevertheless, the previous study has shown that the temporal sampling frequency can also influence evaluating the quality of SM retrievals (Al-Yaari et al., 2019).

To demonstrate the reliability of the conR and the TCR derived here in terms of the impacts from the sampling, the CI were estimated and analyzed by estimating the CI via the resampling based on the randomly one-year blocks. As shown in Fig. 4, the CIs for the conR and the TCR in this study are mostly around 0.1 except the high-latitude regions. Compared to the passive remote-sensing SM products, the CIs of the ASCAT are relatively larger. Generally, the conR and the TCR values used here are affected by sampling procedures to a limited extent when the minimum observations over one-year period is set as 30.

It should be stressed that the conR is strongly dependent on and influenced by the quality of the reference. According to Dong et al. (2020), over some certain LC types, SMOS-IC slightly outperformed the reanalysis products in terms of temporal correlation. Therefore, the marginal underestimation of the temporal performances of the satellite-based products possibly occurs in some areas only when considering the conR.

4.3. Correlations across selected conditions

Since the performances of the SM retrievals from remotely sensed observations vary under different spatial settings, an investigation of

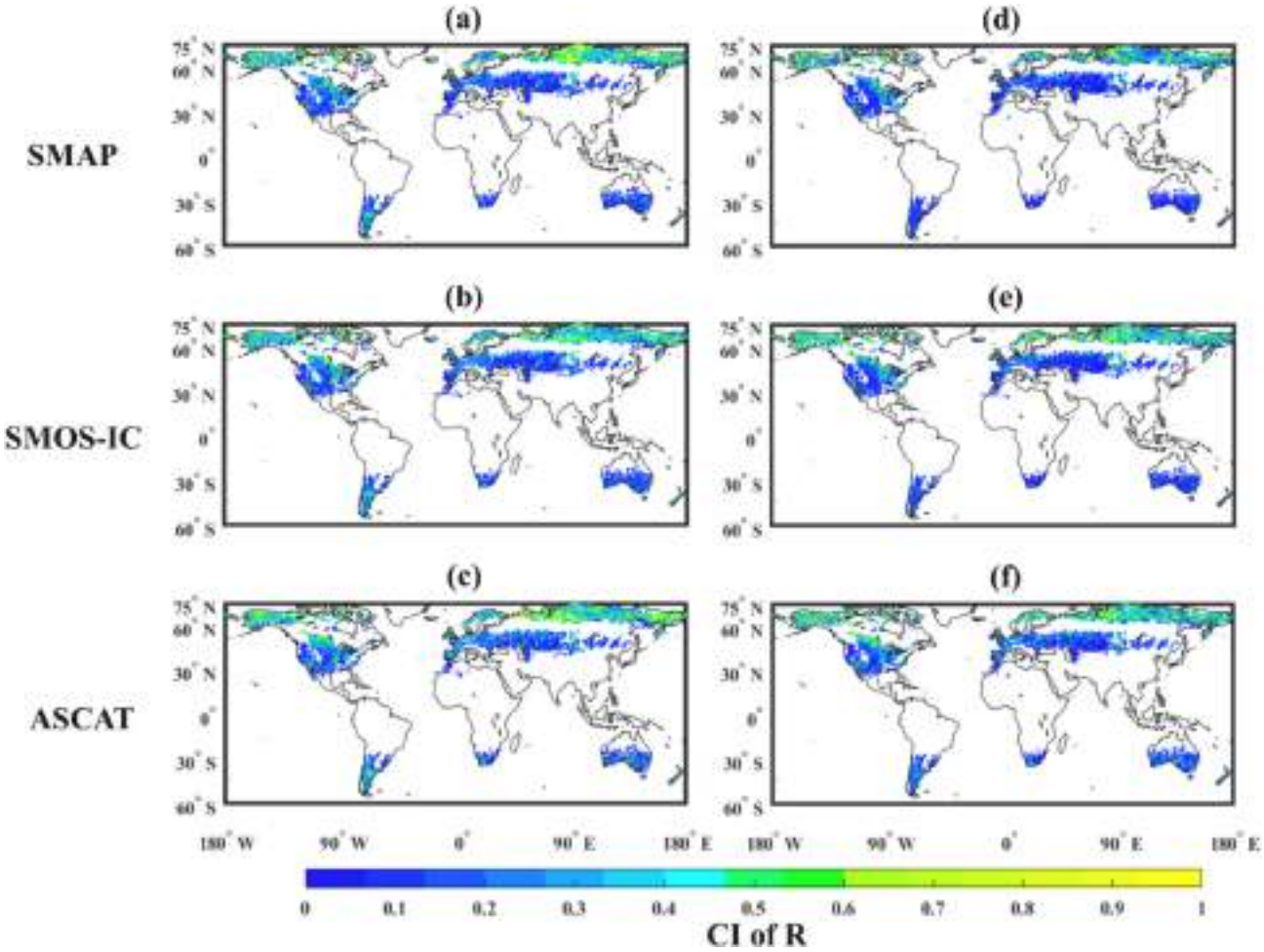

Fig. 4. Global distribution of the confidence intervals (CI) of the conventional R using ERA-Interim for (a) SMAP, (b) SMOS-IC, and (c) ASCAT, as well as the TC-based R for (d) SMAP, (e) SMOS-IC, and (f) ASCAT via resampling.

the temporal performances of different datasets over specific regions is necessary. In addition to recognizing the accuracy of SMAP, SMOS-IC, and ASCAT in a particular class of areas, this facilitates the exploration of reasons leading to the performance difference. Given that the different amplitudes of variations of the R values and the optimal weights may complicate the understanding of the evaluation results, the main text only focuses on the TCR and the conR. The distributions of their derived highest optimal weights are consistent with the R values and are provided in the Supplementary Materials. Here, three important static factors related to the algorithm parameters and SM variations are considered, which are climate zone (CZ), land cover (LC), and mean vegetation water content (VWC).

4.3.1. Climate zone

Firstly, global CZ is provided by an updated global map of the Koppen-Geiger climate classification (Peel et al., 2007). The climate classifications in this map involve five major climatic types including Tropical, Arid, Temperate, Cold, and Polar, and can be further categorized into 30 sub-classes according to the local status of temperature and precipitation. The secondary classification of CZ has been adopted here: Tropical (Af: rainforest, Am: tropical monsoon, Aw: tropical savannah); Arid (BW: arid desert; BS: arid steppe); Temperate (Cs: temperate with dry summer; Cw: temperate with dry winter; Cf: temperate without dry season); Cold (Ds: cold with dry summer; Dw: cold with dry winter; Df: cold without dry season); Polar (ET: polar tundra, EF: polar frost).

Fig. 5 describes the distributions of R values under different climate conditions. Note that the rainforest regions (Af) are only shown for the conventional R because of the small number of samples in the TC-based R.

In general, the TCR values (Fig. 5b) are overestimated compared to those from conR (Fig. 5a), but their ranking patterns are similar to each other. It should be noted that negative signs in the conR broadly appear while the signs of the TCR are generally positive. In particular, the interquartile range of ASCAT is fairly well distributed in the regions exhibiting negative values over Arid, Cold and Polar climate conditions. Therefore, together with estimating the magnitude of R, the sign of the TCR should be reasonably determined by which the optimal weight can be estimated more accurately.

In case of the conR (Fig. 5a), the SMAP and SMOS-IC products display comparable and better R values higher than 0.6 over most climatic regions. Nevertheless, all three SM products present relatively low correlations in the BW (arid desert) and ET (polar tundra) regions. ASCAT has marginally but consistently better performance than SMOS-IC and SMAP products over tropical areas. This result is consistent with the previous study that demonstrates ASCAT has better correlations with the in-situ measurements over the Equatorial climate (Al-Yaari et al., 2019). For the BW condition (desert), SMOS-IC and SMAP can better capture the SM dynamics, which conforms with the conclusions of Wagner et al. (2013). Although the derivation of SMOS-IC relies on the multi-angular and dual-polarization brightness temperatures and has potential of error propagation from the measurement inaccuracy (O'Neill et al., 2015), over the temperate and cold regions, SMAP and SMOS-IC exhibit overall comparable and better performances than

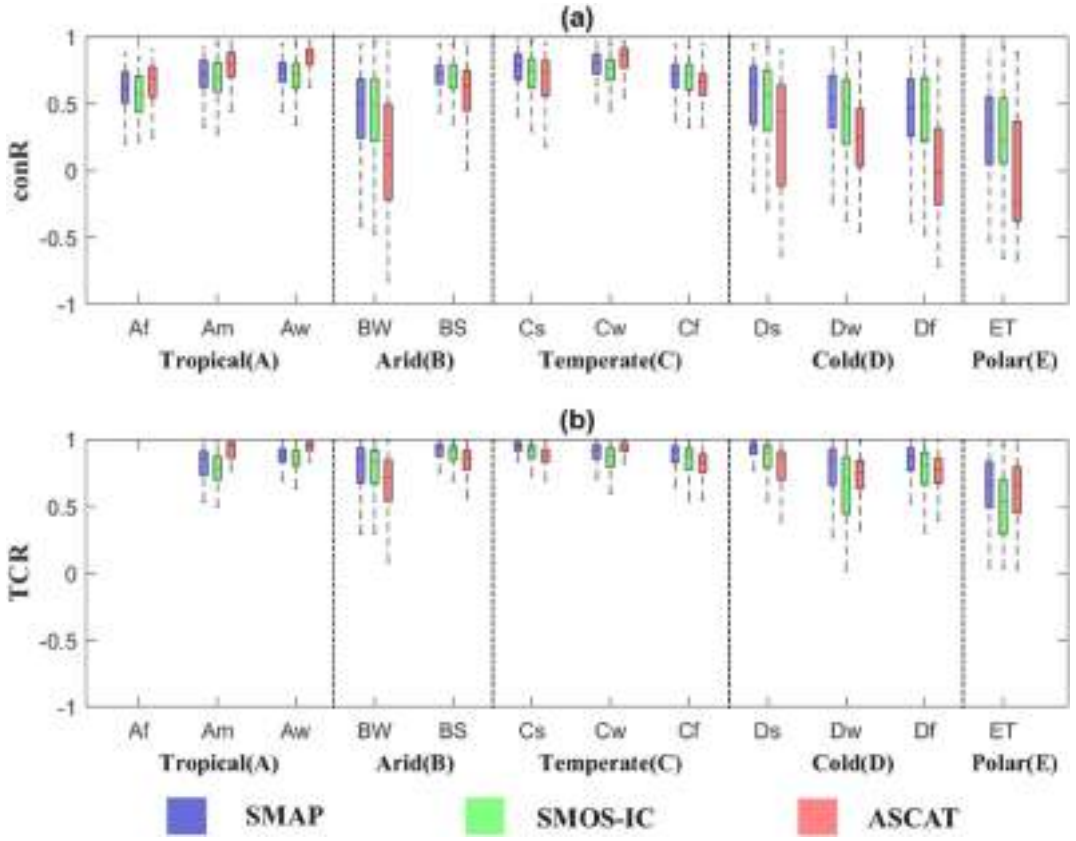

Fig. 5. Boxplots showing variations in the conventional R (a) against ERA-interim and TC-based R (b) under different climate zones. Tropical (Af: rainforest, Am: tropical monsoon, Aw: tropical savannah). Arid (BW: arid desert; BS: arid steppe). Temperate (Cs: temperate with dry summer; Cw: temperate with dry winter; Cf: temperate without dry season). cold and polar (Ds: cold with dry summer; Dw: cold with dry winter; Df: cold without dry season; ET: polar tundra).

ASCAT except for Cw (temperate with dry winter). Furthermore, the temporal performance of ASCAT is sharply degraded over the cold and polar regions.

4.3.2. Land cover

Fig. 6 presents the distribution of R values of SMAP, SMOS-IC, and ASCAT under various LC conditions using boxplots. Here, the map of vegetation types is represented by an MCD12C1 (Version051) product (Friedl et al., 2010) based on the 17-class IGBP classification (Loveland and Belward, 1997) from MODIS observations. Specifically, the IGBP classification includes: ENF (evergreen needleleaf forests); EBF (evergreen broadleaf forests); DNF (deciduous needleleaf forests); DBF (deciduous broadleaf forests); MF (mixed forests); CS (closed shrublands); OS (open shrublands) (OS); WS (woody savannas); S (savannas); PW (permanent wetlands); G (Grassland); C (croplands); UBL (urban and built-up lands); CNV (cropland and natural vegetation mosaics); SI (snow and ice); BSV (barren and sparsely vegetated areas); W (water).

Similarly, the characteristics of the temporal performances represented by the TCR and conR, are overall consistent. Due to the sufficient samples spanning across various LC types, more forest regions are included in Fig. 6a. In general, SMAP and SMOS-IC have superior performance than ASCAT over most LC conditions. However, ASCAT exhibits advantages in savannas regions (WS and S) that typically correspond to the tropical zone. The strength of ASCAT in savannas can be attributed to the high sensitivity of the active microwave instrument to SM over sparsely vegetated areas (Wagner et al., 2013). It seems that all products have difficulty to capture the temporal SM variations over the DNF (deciduous needleleaf forest) and BSV (barren and sparsely vegetated) areas. The poor temporal performances in the regions of DNF may partly account for the lower R values in the high-latitude areas. In contrast to the SM retrievals from ASCAT of which R values greatly fluctuate with varying LC types, the temporal performances of the passive remote sensing SM data are relatively stable and comparable. Dong et al. (2020) showed that SMOS-IC has a stronger ability in capturing the temporal variations of the SM climatology than several land surface modeling products over cropland. In light of this, the conR values of SMOS-IC and even SMAP over certain LC terrains may be slightly underestimated when selecting the modeling products as the references.

4.3.3. Mean vegetation water content

Fig. 7 illustrates the distribution of R values of the satellite-based observation products across various VWC intervals. The average VWC values over the study period have been computed and mapped using the VWC data from the SMAP ancillary datasets (Chan et al., 2013).

SMAP and SMOS-IC have better temporal performances than ASCAT product from 0 to 2 kg/m^2. However, the superior magnitudes change with the variations of VWC. The largest discrepancies between the passive and active remote sensing SM data occur in the VWC intervals of 0–0.4 kg/m^2 and 1.2–1.6 kg/m^2. Such abrupt performance degradation of ASCAT over the moderate vegetation regions (1.2–1.6 kg/m^2) is consistent with Al-Yaari et al. (2019) which indicated that the performance of ASCAT would degrade over the vegetation range with Leaf Aare Index (LAI) from 0 to 3 m^2/m^2. Here, 3 m^2/m^2 of LAI can be approximated to 1.5 kg/m^2 of VWC (Wigneron et al., 2006), corresponding to the ASCAT decline interval in this study. However, ASCAT is more advantageous than SMAP and SMOS-IC over regions with 2–5 kg/m^2 of VWC. This result matches Kim et al. (2018) claiming that ASCAT data have the capacity to accurately reproduce the SM temporal pattern in areas with high vegetation density, considering vegetation optical depth (VOD) from 0 to 0.6. Here, the VOD range from 0 to 0.6 can be approximately as the VWC ranging from 0 to 6 kg/m^2. Lastly, the

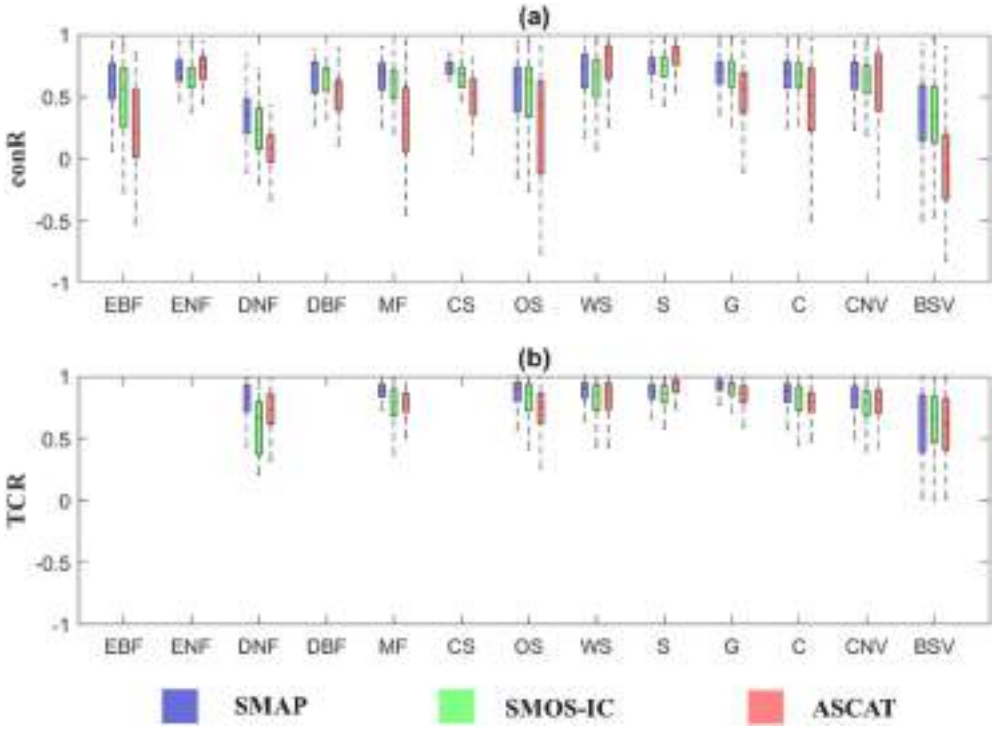

Fig. 6. Boxplots showing variations in the conventional R (a) against ERA-interim and TC-based R (b) under different land cover conditions. EBF (evergreen broadleaf forests); ENF (evergreen needleleaf forests); DNF (deciduous needleleaf forests); DBF (deciduous broadleaf forests); MF (mixed forests); CS (closed shrublands); OS (open shrublands) (OS); WS (woody savannas); S (savannas);G (grassland); C (croplands); CNV (cropland and natural vegetation mosaics); BSV (barren and sparsely vegetated areas).

R values of SMAP, SMOS-IC, and ASCAT become closer over 4–5 kg/m^2 of VWC.

4.4. Global maps of optimal weight

Fig. 8 illustrates the spatial distribution of the best product with the highest optimal weight (w) in terms of maximizing R using ERA-Interim (w_{con}) and the SM truth (w_{TC}) as the objective products. The line plots in the right-hand panel present the variations of zonal mean and one standard deviation of the optimal weights along with the latitude for each parent product. It should be stressed that the w_{TC} was calculated based on Eq. (4) rather than Eq. (6) since the underlying TC assumptions cannot be fully satisfied while directly using the SM raw data.

Before analyzing their relative temporal performances, the consistency between the optimal weights and the R values has been examined. The Spearman correlations between the w_{TC} (w_{con}) and the TCR (conR) are 0.83 (0.71), 0.75 (0.72), and 0.77 (0.65) for SMAP, SMOS-IC, and ASCAT. Compared to the results from the synthetic experiments in the Appendix, the correlations have slightly declined. In terms of the relatively lower Spearman correlations under the reference condition,

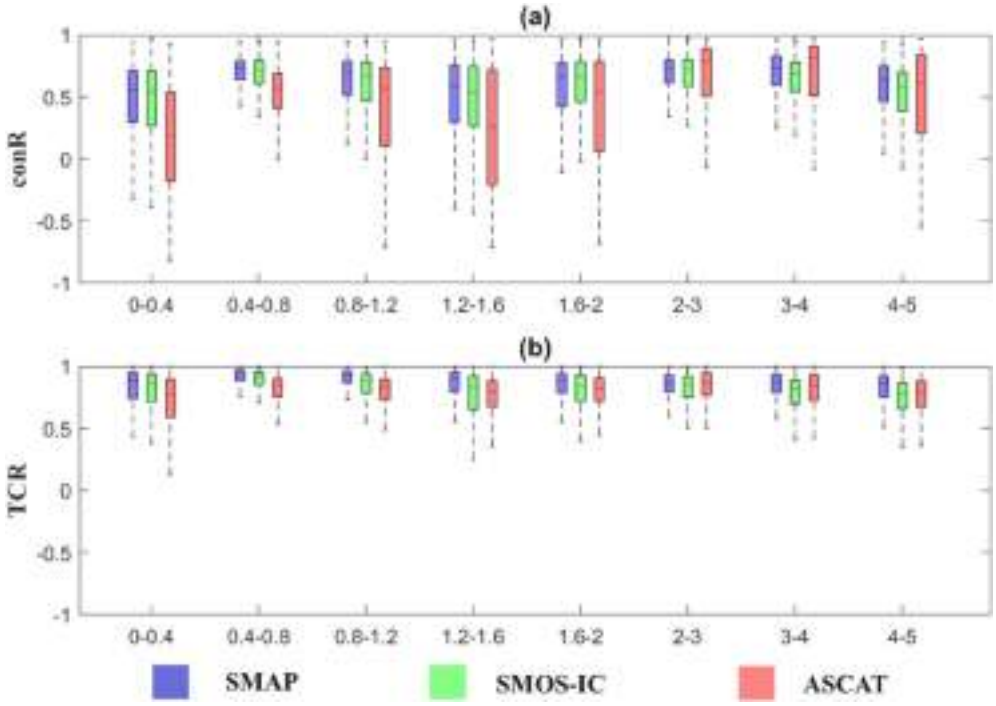

Fig. 7. Boxplots showing variations in the conventional R (a) against ERA-interim and TC-based R (b) under different mean VWC ranges in kg/m^2.

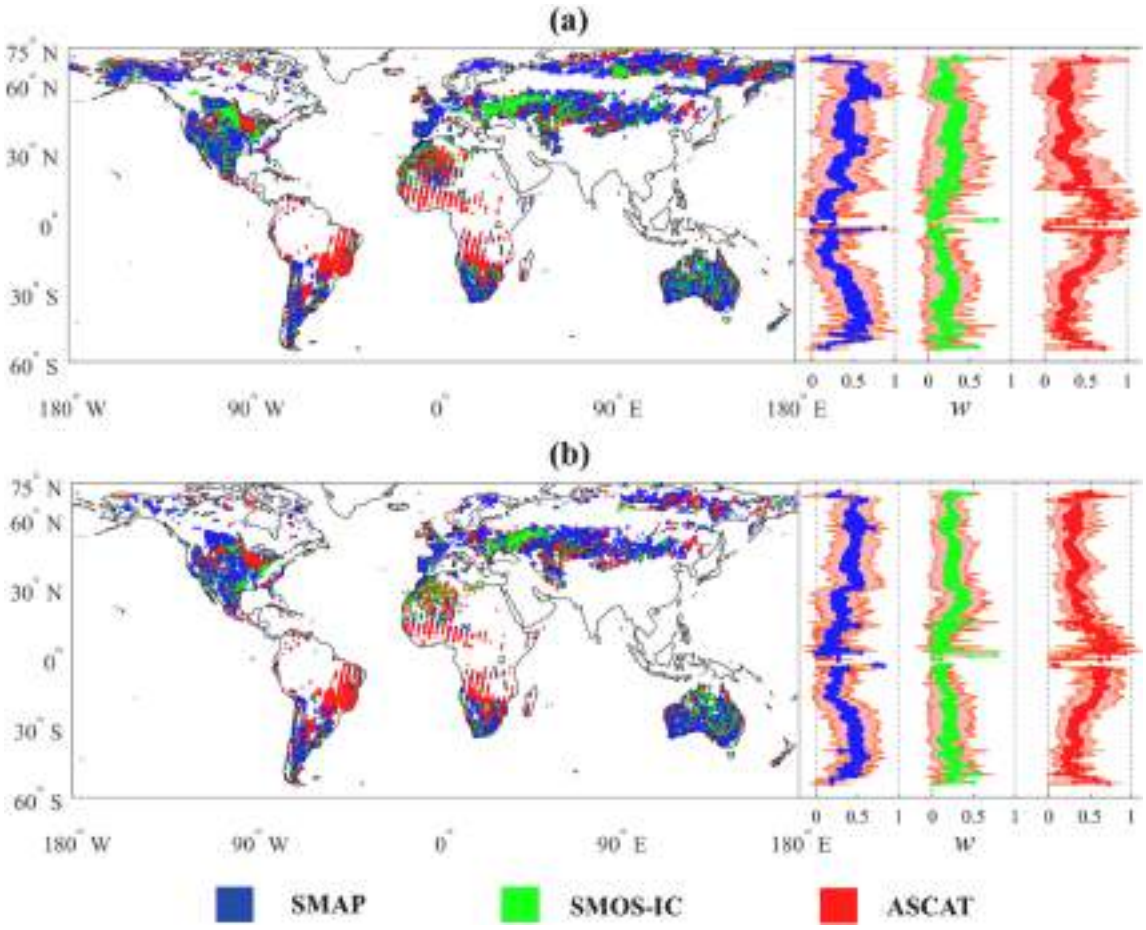

Fig. 8. Global maps indicating areas exhibiting the highest optimal weight (w) for SMAP, SMOS-IC and ASCAT based on (a) w_{con} and (b) w_{TC}. The line plots in the right-hand panel present variations of zonal mean optimal weights with ± 1 standard deviation.

this could be caused by the simultaneous use of the positive and negative conR values, resulting in the unpredictable performance sequences reflected through the w_{con}. Moreover, the correspondences between the highest R and the highest optimal weights are separately 93% (w_{TC} and TCR) and 86% (w_{con} and conR). Therefore, the highest optimal weight can represent the best dataset with the highest contribution to capture the temporal variability of SM.

The complementarity among the SM products can be observed across the geographical areas. The spatial patterns of the highest w_{con} and w_{TC} are overall consistent. The advantageous areas of SMAP include the middle part of North America, most areas in Eurasia, western South America, and southern Africa while SMOS-IC has relatively better performance over eastern North America, several regions in Asia as well as middle Australia. Additionally, ASCAT shows superior performance in eastern South America and most regions in Africa. The latter result is consistent with Al-Yaari et al. (2019) indicating that ASCAT has higher correlations against the in-situ measurements (9 stations) in Africa than SMAP and SMOS products. Furthermore, the advantageous areas of SMAP and ASCAT showing in Fig. 8 are similar to Kim et al. (2018) that compared the performance of SMAP, AMSR2, and ASCAT using the TC approach.

According to Table 4, SMAP and ASCAT have more the highest w_{TC} than SMOS-IC. In terms of the w_{con}, the amounts of grids where the SMAP, SMOS-IC, and ASCAT have the highest optimal weights are comparable. The high proportion of ASCAT with the highest optimal weights can be partially attributed to its negatively high R values distributed over the high-latitude regions and North Africa. In light of this, containing some certain areas where all three products have poor or contrasted performances is likely to affect the overall performance evaluation of a dataset. In a view of visual inspection, however, the advantageous regions of SMAP product cover more diverse areas on a global scale.

Table 4
Proportions (%) of highest weights of three parent products by different references, where the numbers in brackets are the number of pixels.

Reference or its corresponding triplets	SMAP	SMOS-IC	ASCAT	Total
ERA-Interim (w_{con})	34 (18614)	32 (17495)	34 (18653)	100 (54762)
TC (ERA-Interim) (w_{TC})	47 (8935)	21 (3953)	32 (6128)	100 (19016)
MERRA2 (w_{con})	30 (16243)	31 (16879)	39 (21651)	100 (54773)
TC (MERRA2) (w_{TC})	41 (6619)	18 (2899)	42 (6788)	100 (16306)
Average	38	26	37	100

If similar performances of a product (e.g. SMAP) over a certain geographical area or an equivalent static condition were found using different products (ERA-Interim and the SM truth), the results are expected to be more reliable. Here, similar performances can be roughly evaluated from the degree of proximity in the obtained R or optimal weight, and their rank-order variations or one dataset compared to the other two products. Both the conR and TCR values derived based on the ERA-Interim (Fig. 3) and MERRA2 (Fig. S2) are also close. In terms of the zonal mean optimal weights (the right panels of Fig. 8 and Fig. S6), the varying patterns of the zonal optimal weights and their standard deviations are similar in the two cases that applied MERRA2 and ERA-Interim as the references.

When it comes to rank-order variations using MERRA2, the advantaged regions of SMOS-IC are further extended to partial Asia and western Australia (Fig. S6: both conR and TCR calculated using the MERRA2). Given the highly consistent spatial distributions of w_{con} and w_{TC} derived using the same reanalysis product (reference or triplet component), such dissimilar performances are mainly due to the inherent differences in the two reanalysis products. However, for each parent product, the degree of differences between the advantageous regions described by the w_{con} and w_{TC} calculated using the ERA-Interim and MERRA2, is expected to be acceptable. SMAP and SMOS-IC displayed highly comparable and stable temporal performances at a global scale and therefore, the rank order of their approximate R values possibly altered when applying different reanalysis products.

4.5. Limitations and outlook

It should be noted that there are some limitations to this study. Firstly, the above results and discussions are based on SM datasets over a full three-year period from April 1, 2015, to March 31, 2018. SM data covering longer periods are required to evaluate the performance of remotely sensed SM products more accurately and prove the consistency of the results, especially for the TC estimation.

In addition, the SMOS-IC and ASCAT products being compared were first resampled to the SMAP standard spatial resolution (36-km EASE here), and then all products rescaled to the references by a linear normalization approach (Draper et al., 2009). The implementations of these processes inevitably impact the results of inter-comparisons. Furthermore, for the references, only the data nearest to 6 a.m. were selected and used. Hence, the performance of ASCAT in which ascending SM retrievals are normally obtained at 9:30 a.m. may be slightly degraded.

Lastly, this paper only investigated the impacts on the temporal performances of parent products for static conditions without considering influences caused by dynamic factors. Static conditions are mostly defined by average values and cannot reflect the dynamic quality of SM retrievals precisely (Zhang et al., 2019). Given this, the effects on temporal correlations and their derived optimal weights by dynamic factors such as land surface temperature and soil wetness should be investigated in future studies. Moreover, for each grid, the numerical relationship between the optimal weights and dynamic conditions has the potential to combine near-real-time merged products that effectively leverage the strengths of various SM products over certain pixels.

5. Summary and conclusions

This study compared three advanced satellite-based SM products (SMAP, SMOS-IC, and ASCAT) at a global scale in terms of temporal correlations against the reference products (in-situ SM, ERA-Interim, and MERRA2) using the conventional R, TC-based data-truth R values, and their derived optimal weights (w_{con} and w_{TC}). Compared to the R values that independently reflect the temporal performances of the satellite-based SM products with respect to reference products, the optimal weights represent the relative performance of one dataset dependent on the other considered parent products in a comparable manner using normalization. In addition to demonstrating the temporal performances on the rank order, the numerical values of the optimal weights show a wide range of change with the unique information contained in the observation products. Specifically, the high error cross-correlation between two observation products with approximate R values can purposely reduce the contribution from the product with poorer temporal performance to inhibit the impacts from the overlapped errors.

Firstly, the conventional R and the TC-based R calculated using the in-situ measurements and ERA-Interim were compared and the differences between both types of R commonly exist. Theoretically, the TC-based R is expected to be able to reflect the correlations between the satellite-based SM datasets and the SM truth and thus more accurate than the conventional R strongly dependent on the quality of the references. In practice, however, the accuracy of the TC-based R could be influenced by several factors including the violation of TC assumptions, the sign effects as well as the sampling procedures. As such, the conR is expected to be more reliable than the TCR and in-situ TCR over the pixels with the in-situ stations due to the smaller bias with the in-situ conR. Despite that, for each satellite-based SM product considered here, its temporal performances exhibited by the conR and the TCR are highly consistent in terms of the spatial distribution even adopting different references (ERA-Interim and MERRA2).

Regarding the temporal performance, three datasets suffer challenges in retrieving SM over the arid environment and high-latitude regions. Meanwhile, there are some areas where the temporal performances of the studied products are commonly good, such as the most available regions in North America, South America, and Australia, as well as the middle and south parts of Africa. Compared to ASCAT, the SM retrievals from SMAP and SMOS-IC have shown good abilities to reproduce the SM variations over large areas of Eurasia.

Furthermore, global assessment and inter-comparison of the temporal performances under various conditions including climate, land cover, and mean vegetation water content, were conducted. Again, the conventional R (conventional R derived optimal weight) and the TC-based R values (TC-based R derived optimal weight) have overall consistent distribution patterns across diverse static circumstances. In most climate zones, passive remote sensing SM retrievals exhibit stable and higher R values than ASCAT. Specifically, SMAP and SMOS-IC data present substantial advantages in the desert and polar regions. However, ASCAT shows extremely high R values over tropical zones. Concerning the LC, SMOS-IC and SMAP SM retrievals have strong capabilities to reproduce SM variations within most LC types except the DNF (deciduous needleleaf forest) and BSV (barren and sparsely vegetated regions). Despite the high R values of SMAP and SMOS-IC products over WS (woody savannas) and S (savannas) regions, ASCAT exhibits even better temporal performances. Furthermore, the temporal performances of passive remote sensing SM retrievals have superiority in the regions with the VWC intervals of 0–2 kg/m^2, especially in 0–0.4 kg/m^2 and 1.2–1.6 kg/m^2 whereas ASCAT generally outperforms SMAP and SMOS-IC over the areas with the higher vegetation density (2–5 kg/m^2).

The violation of the underlying TC assumptions, the optimization strategies as well as the simultaneous use of R values with opposite signs can account for the decreased matching between the R and optimal weight. Therefore, a set of synthetic experiments has been designed with the aim to investigate the impacts of the error cross-correlations. According to the results of the synthetic experiments, the moderate and high error cross-correlations can overly extend the distances between the optimal weights of two products with similar R values. Such adjustments can avoid incorporating the overlapped error information contained in the parent products but possibly distort and underestimate the contribution from the signal portion of the product. However, in terms of rank order, the consistency between the R and the optimal weight is rarely affected by the error cross-correlations, which is demonstrated by the Spearman correlations continuously more than 0.9. In practice, the Spearman correlations between the optimal weights and the R values are slightly reduced to around 0.8. Therefore, the highest optimal weights have sufficient capacity to represent the performance of the product with the highest R values. As for the advantageous areas of relative performance expressed by the highest optimal weights, the comparably global complementarity can be noticed even though the advantageous areas of SMAP appears to cover more diverse areas from visual observations.

Through the integrated evaluation of the temporal performances of the three SM products, this study can be a guideline for data users to select proper SM datasets for their research. In addition, understanding

the optimal weights in-depth could be helpful to linearly combine the product with improved temporal representations.

Declaration of Competing Interest

The authors declare that they have no known competing financial interests or personal relationships that could have appeared to influence the work reported in this paper.

The authors declare the following financial interests/personal relationships which may be considered as potential competing interests:

Acknowledgements

This work has been partially supported by Australian Research Council. We are grateful to all contributors to the datasets used in this study.

Appendix A. Results of synthetic experiments

For a further insight on the compatibility between the R and the optimal weight, we implemented an experiment using synthetic datasets. Specifically, a group of time-series data representing the truth values (T) was firstly generated using a lag-1 auto-correlation model of which autocorrelation coefficient is randomly drawn from a uniform distribution from 0 to 1. Then, three sets of observation time-series data (Obs) were created by multiplying with random coefficients (α) from 0 to 1 and adding zero-mean Gaussian random errors (ε) to the truth data (Obs = αT + ε). The variances of the errors were limited to fall in the interval 0 to 0.5. Here, we applied a range of error cross-correlation coefficients from 0 to 0.9 increasing by 0.1 for generating random errors while sequentially increasing dependence among the observations. Since the error cross-correlation coefficients can only be controlled by a product pair, there is an unknown error cross-correlation left when the three sets of error time-series data are generated using the two controlled error cross-correlations. The degree of compatibility degrees between the data-truth R and the optimal weight were estimated using the Spearman rank-order correlation. Furthermore, the highest values (H) of the R and the optimal weight as well as the differences (ΔD) between the highest R (optimal weight) and the second highest R (optimal weight) were compared and discussed. To assess the uncertainty in the results, the synthetic experiment was repeated 1000 times.

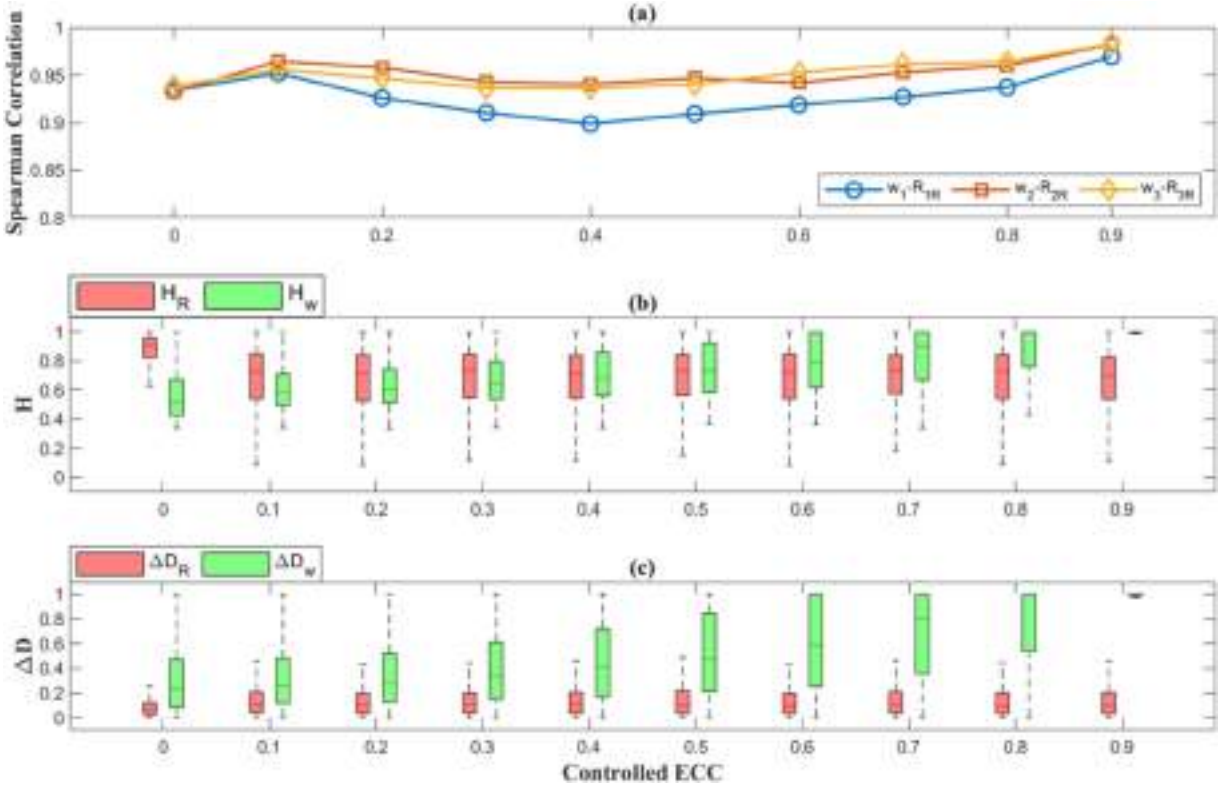

Fig. A1. Results of the synthetic experiments under the controlled error cross-correlations (ECC): (a) Spearman correlations between the R and the optimal weight (b) boxplot of the highest R (H_R) and the highest optimal weights (H_w) (c) the differences (ΔD) between the highest and the second highest R values (ΔD_R)or optimal weight values (ΔD_w).

According to the Fig. A1a, the Spearman correlations between the R and the optimal weight are generally higher than 0.9 regardless of the increasing error cross-correlations. Therefore, the optimal weight has the ability to represent the relative temporal performance of each parent product consistent with the R values. However, the numerical values of the optimal weight can be impacted by the error cross-correlations. With the increase of the error cross-correlations, the highest optimal weights rise to closer to 1 no matter what the highest R values are (Fig. A1b). Additionally, ΔD values of the optimal weights are inclined to rapidly expand once the controlled error cross-correlations are larger than 0.3 (Fig. A1c). In light of this, the optimal weights and the combined product are likely to excessively rely on the parent product with the best performance. While the controlled error cross-correlations are near 0.9, the optimal weights are mostly concentrated to either 1 or 0. The values under such extreme conditions indicate that the optimal weights can accordingly adjust to avoid overlapping error information from different parent products. Given that, the signal portions of the parent products are also likely to have certain impacts on the optimal weights in a similar manner but at a greatly reduced magnitude. However, the exaggerated values of the highest optimal weights are likely to block the signal portions of the other parent products and underestimate their respective contributions. As a result, the optimal weight can describe the relative temporal performance consistent

with the R, avoid the overlapping error information from different parent products in the combination, and have the potential to perform as an indicator of the error cross-correlations.

References

Albergel, C., Rüdiger, C., Pellarin, T., Calvet, J.-C., Fritz, N., Froissard, F., Suquia, D., Petitpa, A., Piguet, B., Martin, E., 2008. From near-Surface to Root-Zone Soil Moisture Using an Exponential Filter: An Assessment of the Method Based on In-Situ Observations and Model Simulations.

Al-Yaari, A., Wigneron, J.-P., Ducharne, A., Kerr, Y., De Rosnay, P., De Jeu, R., Govind, A., Al Bitar, A., Albergel, C., Munoz-Sabater, J., 2014. Global-scale evaluation of two satellite-based passive microwave soil moisture datasets (SMOS and AMSR-E) with respect to land data assimilation system estimates. Remote Sens. Environ. 149, 181–195.

Al-Yaari, A., Wigneron, J.-P., Dorigo, W., Colliander, A., Pellarin, T., Hahn, S., Mialon, A., Richaume, P., Fernandez-Moran, R., Fan, L., 2019. Assessment and inter-comparison of recently developed/reprocessed microwave satellite soil moisture products using ISMN ground-based measurements. Remote Sens. Environ. 224, 289–303.

Bell, J.E., Palecki, M.A., Baker, C.B., Collins, W.G., Lawrimore, J.H., Leeper, R.D., Hall, M.E., Kochendorfer, J., Meyers, T.P., Wilson, T., 2013. US climate reference network soil moisture and temperature observations. J. Hydrometeorol. 14, 977–988.

Bertoldi, G., Della Chiesa, S., Notarnicola, C., Pasolli, L., Niedrist, G., Tappeiner, U., 2014. Estimation of soil moisture patterns in mountain grasslands by means of SAR RADARSAT2 images and hydrological modeling. J. Hydrol. 516, 245–257.

Bircher, S., Skou, N., Jensen, K.H., Walker, J.P., Rasmussen, L., Verhoest, N., 2012. A soil moisture and temperature network for SMOS validation in Western Denmark. Hydrol. Earth Syst. Sci. 16.

Brocca, L., Melone, F., Moramarco, T., Morbidelli, R., 2009a. Soil moisture temporal stability over experimental areas in Central Italy. Geoderma 148, 364–374.

Brocca, L., Melone, F., Moramarco, T., Singh, V., 2009b. Assimilation of observed soil moisture data in storm rainfall-runoff modeling. J. Hydrol. Eng. 14, 153–165.

Brodzik, M.J., Billingsley, B., Haran, T., Raup, B., Savoie, M.H., 2012. EASE-grid 2.0: incremental but significant improvements for earth-gridded data sets. ISPRS Int. J. Geo Inf. 1, 32–45.

Chan, S., Hunt, R., Bindlish, R., Njoku, E., Kimball, J., Jackson, T., 2013. SMAP ancillary data report: vegetation water content. In: Jet Propulsion Lab., California Inst. Technol., Pasadena, CA, USA, JPL D-53058.

Chen, F., Crow, W.T., Bindlish, R., Colliander, A., Burgin, M.S., Asanuma, J., Aida, K., 2018. Global-scale evaluation of SMAP, SMOS and ASCAT soil moisture products using triple collocation. Remote Sens. Environ. 214, 1–13.

Clewley, D., Whitcomb, J.B., Akbar, R., Silva, A.R., Berg, A., Adams, J.R., Caldwell, T., Entekhabi, D., Moghaddam, M., 2017. A method for Upscaling in situ soil moisture measurements to satellite footprint scale using random forests. IEEE J. Sel. Topics Appl. Earth Obs. Remote Sens. 10, 2663–2673.

Colliander, A., Jackson, T.J., Chan, S., O'Neill, P., Bindlish, R., Cosh, M., Caldwell, T., Walker, J., Berg, A., McNairn, H., 2018. An assessment of the differences between spatial resolution and grid size for the SMAP enhanced soil moisture product over homogeneous sites. Remote Sens. Environ. 207, 65–70.

Crow, W.T., Berg, A.A., Cosh, M.H., Loew, A., Mohanty, B.P., Panciera, R., de Rosnay, P., Ryu, D., Walker, J.P., 2012. Upscaling sparse ground-based soil moisture observations for the validation of coarse-resolution satellite soil moisture products. Rev. Geophys. 50, RG2002.

De Lannoy, G.J., Koster, R.D., Reichle, R.H., Mahanama, S.P., Liu, Q., 2014. An updated treatment of soil texture and associated hydraulic properties in a global land modeling system. J. Adv. Model. Earth Syst. 6, 957–979.

Dee, D.P., Uppala, S.M., Simmons, A., Berrisford, P., Poli, P., Kobayashi, S., Andrae, U., Balmaseda, M., Balsamo, G., Bauer, d.P., 2011. The ERA-interim reanalysis: configuration and performance of the data assimilation system. Q. J. R. Meteorol. Soc. 137, 553–597.

Dong, J., Crow, W.T., Tobin, K.J., Cosh, M.H., Bosch, D.D., Starks, P.J., Seyfried, M., Collins, C.H., 2020. Comparison of microwave remote sensing and land surface modeling for surface soil moisture climatology estimation. Remote Sens. Environ. 242, 111756.

Dorigo, W.A., Scipal, K., Parinussa, R.M., Liu, Y.Y., Wagner, W., De Jeu, R.A., Naeimi, V., 2010. Error characterisation of global active and passive microwave soil moisture datasets. Hydrol. Earth Syst. Sci. 14, 2605.

Dorigo, W.A., Wagner, W., Hohensinn, R., Hahn, S., Paulik, C., Xaver, A., Gruber, A., Drusch, M., Mecklenburg, S., van Oevelen, P., Robock, A., Jackson, T., 2011. The international soil moisture network: a data hosting facility for global in situ soil moisture measurements. Hydrol. Earth Syst. Sci. 15, 1675–1698.

Dorigo, W., Gruber, A., De Jeu, R., Wagner, W., Stacke, T., Loew, A., Albergel, C., Brocca, L., Chung, D., Parinussa, R., 2015. Evaluation of the ESA CCI soil moisture product using ground-based observations. Remote Sens. Environ. 162, 380–395.

Draper, C.S., Walker, J.P., Steinle, P.J., De Jeu, R.A., Holmes, T.R., 2009. An evaluation of AMSR–E derived soil moisture over Australia. Remote Sens. Environ. 113, 703–710.

Entekhabi, D., Rodriguez-Iturbe, I., Castelli, F., 1996. Mutual interaction of soil moisture state and atmospheric processes. J. Hydrol. 184, 3–17.

Entekhabi, D., Asrar, G.R., Betts, A.K., Beven, K.J., Bras, R.L., Duffy, C.J., Dunne, T., Koster, R.D., Lettenmaier, D.P., McLaughlin, D.B., 1999. An agenda for land surface hydrology research and a call for the second international hydrological decade. Bull. Am. Meteorol. Soc. 80, 2043–2058.

Entekhabi, D., Njoku, E.G., O'Neill, P.E., Kellogg, K.H., Crow, W.T., Edelstein, W.N., Entin, J.K., Goodman, S.D., Jackson, T.J., Johnson, J., 2010a. The soil moisture active passive (SMAP) mission. Proc. IEEE 98, 704–716.

Entekhabi, D., Reichle, R.H., Koster, R.D., Crow, W.T., 2010b. Performance metrics for soil moisture retrievals and application requirements. J. Hydrometeorol. 11, 832–840.

De Jeu, R.d., & EOwe, M. (2003). Further validation of a new methodology for surface moisture and vegetation optical depth retrieval. Int. J. Remote Sens., 24, 4559–4578.

Fernandez-Moran, R., Al-Yaari, A., Mialon, A., Mahmoodi, A., Al Bitar, A., De Lannoy, G., Rodriguez-Fernandez, N., Lopez-Baeza, E., Kerr, Y., Wigneron, J.-P., 2017a. SMOS-IC: an alternative SMOS soil moisture and vegetation optical depth product. Remote Sens. 9, 457.

Fernandez-Moran, R., Wigneron, J.-P., De Lannoy, G., Lopez-Baeza, E., Parrens, M., Mialon, A., Mahmoodi, A., Al-Yaari, A., Bircher, S., Al Bitar, A., 2017b. A new calibration of the effective scattering albedo and soil roughness parameters in the SMOS SM retrieval algorithm. Int. J. Appl. Earth Obs. Geoinf. 62, 27–38.

Friedl, M.A., Sulla-Menashe, D., Tan, B., Schneider, A., Ramankutty, N., Sibley, A., Huang, X., 2010. MODIS collection 5 global land cover: algorithm refinements and characterization of new datasets. Remote Sens. Environ. 114, 168–182.

Gruber, A., Su, C.H., Zwieback, S., Crow, W., Dorigo, W., Wagner, W., 2016. Recent advances in (soil moisture) triple collocation analysis. Int. J. Appl. Earth Obs. Geoinformation 45, 200–211 Part B.

Guillod, B.P., Orlowsky, B., Miralles, D.G., Teuling, A.J., Seneviratne, S.I., 2015. Reconciling spatial and temporal soil moisture effects on afternoon rainfall. Nat. Commun. 6, 6443.

Gupta, P., Christopher, S.A., Wang, J., Gehrig, R., Lee, Y., Kumar, N., 2006. Satellite remote sensing of particulate matter and air quality assessment over global cities. Atmos. Environ. 40, 5880–5892.

Hagan, D.F.T., Wang, G., Kim, S., Parinussa, R.M., Liu, Y., Ullah, W., Bhatti, A.S., Ma, X., Jiang, T., Su, B., 2020. Maximizing temporal correlations in long-term global satellite soil moisture data-merging. Remote Sens. 12, 2164.

Hahn, S., 2016. Algorithm theoretical baseline document (ATBD) surface soil moisture ASCAT data record time series. In: Tech. Rep. Doc. No: SAF/HSAF/CDOP2/ATBD, v0.4.

Holmes, T., De Rosnay, P., De Jeu, R., Wigneron, R.P., Kerr, Y., Calvet, J.C., Escorihuela, M., Saleh, K., Lemaître, F., 2006. A new parameterization of the effective temperature for L band radiometry. Geophys. Res. Lett. 33.

Kerr, Y.H., 2007. Soil moisture from space: where are we? Hydrogeol. J. 15, 117–120.

Kerr, Y.H., Waldteufel, P., Wigneron, J.-P., Martinuzzi, J., Font, J., Berger, M., 2001. Soil moisture retrieval from space: the soil moisture and ocean salinity (SMOS) mission. IEEE Trans. Geosci. Remote Sens. 39, 1729–1735.

Kerr, Y.H., Waldteufel, P., Richaume, P., Wigneron, J.P., Ferrazzoli, P., Mahmoodi, A., Al Bitar, A., Cabot, F., Gruhier, C., Juglea, S.E., 2012. The SMOS soil moisture retrieval algorithm. IEEE Trans. Geosci. Remote Sens. 50, 1384–1403.

Kerr, Y., Wigneron, J.-P., Al Bitar, A., Mialon, A., Srivastava, P., 2016. Soil moisture from space: techniques and limitations. Satell. Soil Moisture Retrieval 3–27 Elsevier.

Kim, S., Parinussa, R.M., Liu, Y.Y., Johnson, F.M., Sharma, A., 2015. A framework for combining multiple soil moisture retrievals based on maximizing temporal correlation. Geophys. Res. Lett. 42, 6662–6670.

Kim, S., Parinussa, R.M., Liu, Y.Y., Johnson, F.M., Sharma, A., 2016. Merging alternate remotely-sensed soil moisture retrievals using a non-static model combination approach. Remote Sens. 8, 518.

Kim, H., Parinussa, R., Konings, A.G., Wagner, W., Cosh, M.H., Lakshmi, V., Zohaib, M., Choi, M., 2018. Global-scale assessment and combination of SMAP with ASCAT (active) and AMSR2 (passive) soil moisture products. Remote Sens. Environ. 204, 260–275.

Kim, S., Zhang, R., Pham, H., Sharma, A., 2019. A Review of Satellite-Derived Soil Moisture and its Usage for Flood Estimation. (Remote Sensing in Earth Systems Sciences).

Koster, R.D., Suarez, M.J., 2001. Soil moisture memory in climate models. J. Hydrometeorol. 2, 558–570.

Leavesley, G., David, O., Garen, D., Lea, J., Marron, J., Pagano, T., Perkins, T., Strobel, M., 2008. A modeling framework for improved agricultural water supply forecasting. In: AGU Fall Meeting Abstracts, p. 0497.

Li, Xiaojun, Al-Yaari, A., Schwank, M., Fan, Lei, Frappart, F., Swenson, J., Wigneron, J.-P., 2020. Compared performances of SMOS-IC soil moisture and vegetation optical depth retrievals based on Tau-Omega and Two-Stream microwave emission models. Remote Sensing of Environment 236https://doi.org/10.1016/j.rse.2019.111502. In this issue.

Loveland, T.R., Belward, A., 1997. The IGBP-DIS global 1km land cover data set, DISCover: first results. Int. J. Remote Sens. 18, 3289–3295.

Ma, H., Zeng, J., Chen, N., Zhang, X., Cosh, M.H., Wang, W., 2019. Satellite surface soil moisture from SMAP, SMOS, AMSR2 and ESA CCI: a comprehensive assessment using global ground-based observations. Remote Sens. Environ. 231, 111215.

McColl, K.A., Vogelzang, J., Konings, A.G., Entekhabi, D., Piles, M., Stoffelen, A., 2014. Extended triple collocation: estimating errors and correlation coefficients with respect to an unknown target. Geophys. Res. Lett. 41, 6229–6236.

Mironov, V.L., Kosolapova, L.G., Fomin, S.V., 2009. Physically and mineralogically based spectroscopic dielectric model for moist soils. IEEE Trans. Geosci. Remote Sens. 47, 2059–2070.

Mo, T., Choudhury, B., Schmugge, T., Wang, J., Jackson, T., 1982. A model for microwave emission from vegetation-covered fields. J. Geophys. Res. Oceans 87, 11229–11237.

Moghaddam, M., Entekhabi, D., Goykhman, Y., Li, K., Liu, M., Mahajan, A., Nayyar, A., Shuman, D., Teneketzis, D., 2010. A wireless soil moisture smart sensor web using physics-based optimal control: concept and initial demonstrations. IEEE J. Sel. Topics Appl. Earth Obs. Remote Sens. 3, 522–535.
Morrison, K., Wagner, W., 2019. Explaining anomalies in SAR and Scatterometer soil moisture retrievals from dry soils with subsurface scattering. IEEE Trans. Geosci. Remote Sens. 58, 2190–2197.
Naeimi, V., Scipal, K., Bartalis, Z., Hasenauer, S., Wagner, W., 2009. An improved soil moisture retrieval algorithm for ERS and METOP scatterometer observations. IEEE Trans. Geosci. Remote Sens. 47, 1999–2013.
NASA-LP-DAAC, 2012. Land cover type yearly L3 Global 0.05Deg CMG. In: NASA LP DACC, USGS EROS Center, Sioux Falls, South Dakota (https://lpdaac.usgs.gov).
Ojo, E.R., Bullock, P.R., L'Heureux, J., Powers, J., McNairn, H., Pacheco, A., 2015. Calibration and evaluation of a frequency domain reflectometry sensor for real-time soil moisture monitoring. Vadose Zone J. 14, 1–12.
O'Neill, P., Njoku, E., Jackson, T., Chan, S., Bindlish, R., 2015. SMAP algorithm theoretical basis document: level 2 & 3 soil moisture (passive) data products. In: Jet Propulsion Lab., California Inst. Technol., Pasadena, CA, USA, JPL D-66480.
O'Neill, P.E., Chan, S., Njoku, E.G., Jackson, T., Bindlish, R., 2018. SMAP L3 Radiometer Global Daily 36 Km EASE-Grid Soil Moisture, Version 5 (SPL3SMP). NASA National Snow and Ice Data Center Distributed Active Archive Center, Boulder, Colorado USA.
Parrens, M., Wigneron, J.-P., Richaume, P., Mialon, A., Al Bitar, A., Fernandez-Moran, R., Al-Yaari, A., Kerr, Y.H., 2016. Global-scale surface roughness effects at L-band as estimated from SMOS observations. Remote Sens. Environ. 181, 122–136.
Peel, M.C., Finlayson, B.L., McMahon, T.A., 2007. Updated World Map of the Köppen-Geiger Climate Classification.
Pellarin, T., Wigneron, J.-P., Calvet, J.-C., Berger, M., Douville, H., Ferrazzoli, P., Kerr, Y.H., Lopez-Baeza, E., Pulliainen, J., Simmonds, L.P., 2003. Two-year global simulation of L-band brightness temperatures over land. IEEE Trans. Geosci. Remote Sens. 41, 2135–2139.
Petropoulos, G.P., Ireland, G., Barrett, B., 2015. Surface soil moisture retrievals from remote sensing: current status, products & future trends. Phys. Chem. Earth Parts A/B/C 83, 36–56.
Reichle, R.H., Koster, R.D., Dong, J., Berg, A.A., 2004. Global soil moisture from satellite observations, land surface models, and ground data: implications for data assimilation. J. Hydrometeorol. 5, 430–442.
Reichle, R.H., Draper, C.S., Liu, Q., Girotto, M., Mahanama, S.P., Koster, R.D., De Lannoy, G.J., 2017. Assessment of MERRA-2 land surface hydrology estimates. J. Clim. 30, 2937–2960.
Sanchez, N., Martínez-Fernández, J., Scaini, A., Perez-Gutierrez, C., 2012. Validation of the SMOS L2 soil moisture data in the REMEDHUS network (Spain). IEEE Trans. Geosci. Remote Sens. 50, 1602–1611.
Srivastava, P.K., Han, D., Ramirez, M.A.R., Islam, T., 2013. Appraisal of SMOS soil moisture at a catchment scale in a temperate maritime climate. J. Hydrol. 498, 292–304.
Srivastava, P.K., Han, D., Rico-Ramirez, M.A., O'Neill, P., Islam, T., Gupta, M., Dai, Q., 2015. Performance evaluation of WRF-Noah land surface model estimated soil moisture for hydrological application: synergistic evaluation using SMOS retrieved soil moisture. J. Hydrol. 529, 200–212.
Stoffelen, A., 1998. Toward the true near-surface wind speed: error modeling and calibration using triple collocation. J. Geophys. Res. Oceans 103, 7755–7766 (1978–2012).
Ulaby, F.T., Moore, R.K., Fung, A.K., 1986. Microwave Remote Sensing: Active and Passive. Volume 3-from Theory to Applications.
Van den Hurk, B.J., Graham, L.P., Viterbo, P., 2002. Comparison of land surface hydrology in regional climate simulations of the Baltic Sea catchment. J. Hydrol. 255, 169–193.
Wagner, W., Lemoine, G., Rott, H., 1999. A method for estimating soil moisture from ERS scatterometer and soil data. Remote Sens. Environ. 70, 191–207.
Wagner, W., Hahn, S., Kidd, R., Melzer, T., Bartalis, Z., Hasenauer, S., Figa-Saldaña, J., de Rosnay, P., Jann, A., Schneider, S., 2013. The ASCAT soil moisture product: a review of its specifications, validation results, and emerging applications. Meteorol. Z. 22, 5–33.
Wigneron, J.-P., Schmugge, T., Chanzy, A., Calvet, J.-C., Kerr, Y., 1998. Use of Passive Microwave Remote Sensing to Monitor Soil Moisture.
Wigneron, J.-P., Waldteufel, P., Chanzy, A., Calvet, J.-C., Kerr, Y., 2000. Two-dimensional microwave interferometer retrieval capabilities over land surfaces (SMOS mission). Remote Sens. Environ. 73, 270–282.
Wigneron, J.-P., Calvet, J.-C., De Rosnay, P., Kerr, Y., 2006. L-MEB: A Simple Model at L-Band for the Continental Areas-Application to the Simulation of a Half-Degree Resolution and Global Scale Data Set. IEE Electromagnetic Waves series.
Wigneron, J.-P., Kerr, Y., Waldteufel, P., Saleh, K., Escorihuela, M.-J., Richaume, P., Ferrazzoli, P., De Rosnay, P., Gurney, R., Calvet, J.-C., 2007. L-band microwave emission of the biosphere (L-MEB) model: description and calibration against experimental data sets over crop fields. Remote Sens. Environ. 107, 639–655.
Wigneron, J.-P., Jackson, T., O'neill, P., De Lannoy, G., De Rosnay, P., Walker, J., Ferrazzoli, P., Mironov, V., Bircher, S., Grant, J., 2017. Modelling the passive microwave signature from land surfaces: a review of recent results and application to the L-band SMOS & SMAP soil moisture retrieval algorithms. Remote Sens. Environ. 192, 238–262.
Yilmaz, M.T., Crow, W.T., 2013. The optimality of potential rescaling approaches in land data assimilation. J. Hydrometeorol. 14, 650–660.
Yilmaz, M.T., Crow, W.T., 2014. Evaluation of assumptions in soil moisture triple collocation analysis. J. Hydrometeorol. 15, 1293–1302.
Zhang, R., Kim, S., Sharma, A., 2019. A comprehensive validation of the SMAP enhanced Level-3 soil moisture product using ground measurements over varied climates and landscapes. Remote Sens. Environ. 223, 82–94.
Zreda, M., Desilets, D., Ferré, T., Scott, R.L., 2008. Measuring soil moisture content non-invasively at intermediate spatial scale using cosmic-ray neutrons. Geophys. Res. Lett. 35.